Economic Geology, v. 115, no. 4, pp. 771–791

Exploration Targeting in Porphyry Cu Systems Using Propylitic Mineral Chemistry: A Case Study of the El Teniente Deposit, Chile

Jamie J. Wilkinson,[1,2,3,†] Michael J. Baker,[3] David R. Cooke,[3] and Clara C. Wilkinson[1,3]

[1]*London Centre for Ore Deposits and Exploration (LODE), Department of Earth Sciences, Natural History Museum, Cromwell Road, London SW7 5BD, United Kingdom*

[2]*Department of Earth Science and Engineering, Imperial College London, Exhibition Road, London SW7 2AZ, United Kingdom*

[3]*Centre for Ore Deposits and Earth Sciences (CODES), University of Tasmania, Private Bag 79, Hobart, Tasmania 7001, Australia*

Abstract

The mineral chemistry of epidote and chlorite from the propylitic halo at El Teniente, in samples collected at distances up to 6.6 km from the deposit center, was determined by microprobe and laser ablation-inductively coupled plasma-mass spectrometry. Results show that both minerals systematically incorporated a range of trace elements that define a much larger footprint to the system than is easily recognized using conventional means such as whole-rock geochemistry. Apart from Fe and Mg in chlorite, there is no significant control of mineral chemistry by bulk-rock composition. For chlorite, geothermometry temperatures and Ti and V concentrations are high proximal, whereas Li, As, Co, Sr, Ca, and Y are low proximal and elevated in distal positions. Ratios of these elements define gradients toward ore varying over three to five orders of magnitude. The proximal-high Ti content is thought to reflect crystallization temperature, whereas proximal-low signatures are believed to characterize elements that are relatively fluid mobile in the inner parts of the propylitic halo in the presence of mildly alkaline to mildly acidic and oxidized fluids so that they are not incorporated into crystallizing chlorite, despite being generally compatible within the mineral structure. These elements begin to substitute into chlorite in the distal parts of the propylitic halo where fluids are largely rock buffered in terms of major element chemistry. In epidote, As defines a broad proximal low and is generally elevated at distances of at least 3 km from the edge of the ore shell. Zinc, La, Yb, Y, and Zr in epidote, among others, appear to define a geochemical shoulder that surrounds the deposit. These patterns are broadly similar to those observed in previous work at Batu Hijau and in the Baguio district, suggesting that these minerals behave consistently in porphyry systems and can therefore provide useful exploration tools within propylitic green rocks.

Introduction

Porphyry ore deposits represent remarkable accumulations of metals—in particular Cu, Mo, and Au—typically precipitated from hydrothermal fluids in an intrusive host and its surrounding country rocks. Deposits are normally centered within an alteration halo with characteristic mineralogical and chemical zoning patterns (Cooke et al., 2014a). This footprint is a key guide for exploration, providing a larger (several km radius) target area within which mineralization may exist.

The most distal alteration facies—the propylitic zone—has been traditionally regarded as a largely isochemical alteration domain (e.g., Sillitoe, 2010) containing little information of use in exploration once beyond the pyrite halo (which may extend into proximal propylitic rocks). Furthermore, the mineral assemblages that characterize propylitic alteration (including actinolite, magnetite, albite, pyrite, epidote, chlorite, sericite, calcite, prehnite, hematite, and zeolites; e.g., Ballantyne, 1981) may be present within barren hydrothermal systems or produced by processes such as regional metamorphism. The lack of research in this environment means that the controls on the formation of these huge alteration zones are incompletely understood. However, because they are so laterally extensive and frequently encountered, an enhanced capability to explore within this domain would be extremely powerful. Indeed, recent work (Cooke et al., 2014b; Wilkinson et al., 2015; Neal et al., 2018; also see Ahmed et al., 2020; Baker et al., 2020; Cooke et al., 2020; Pacey et al., 2020a), part of a series of AMIRA research projects led by the University of Tasmania, has shown that valuable chemical information is locked up in epidote and chlorite that can provide useful exploration insights.

Here, we present the results of a study of the propylitic halo of El Teniente, Chile, one of the largest porphyry Cu-Mo systems known, in order to assess whether previously documented patterns are reproduced and to evaluate whether the alteration mineral chemistry footprint extends beyond that defined by conventional whole-rock geochemistry. We consider the differences between the giant El Teniente Cu-Mo system and previous results from the smaller, Cu-Au porphyry systems studied in the Baguio district, Philippines, Batu Hijau, and Indonesia and also from metamorphic background suites.

El Teniente Geology and Propylitic Alteration

El Teniente is located on the western margin of the Andean Cordillera, approximately 70 km southeast of Santiago, within the confines of the Central Chilean porphyry copper belt. It is the world's largest underground Cu mine, hosting a premining resource of approximately 95 million tonnes (Mt) of fine Cu (Camus, 2002; Stern et al., 2010), and is the world's largest known resource of Mo (Sillitoe, 2010) with a current plus mined resource total of approximately 2.5 Mt (Camus, 2002).

The deposit is hosted by a late Miocene volcano-plutonic complex, the Teniente Mafic Complex, which occurs within the

[†]Corresponding author: e-mail, j.wilkinson@nhm.ac.uk

ISSN 0361-0128; doi:10.5382/econgeo.4738; 21 p.
Digital appendices are available in the online Supplements section.

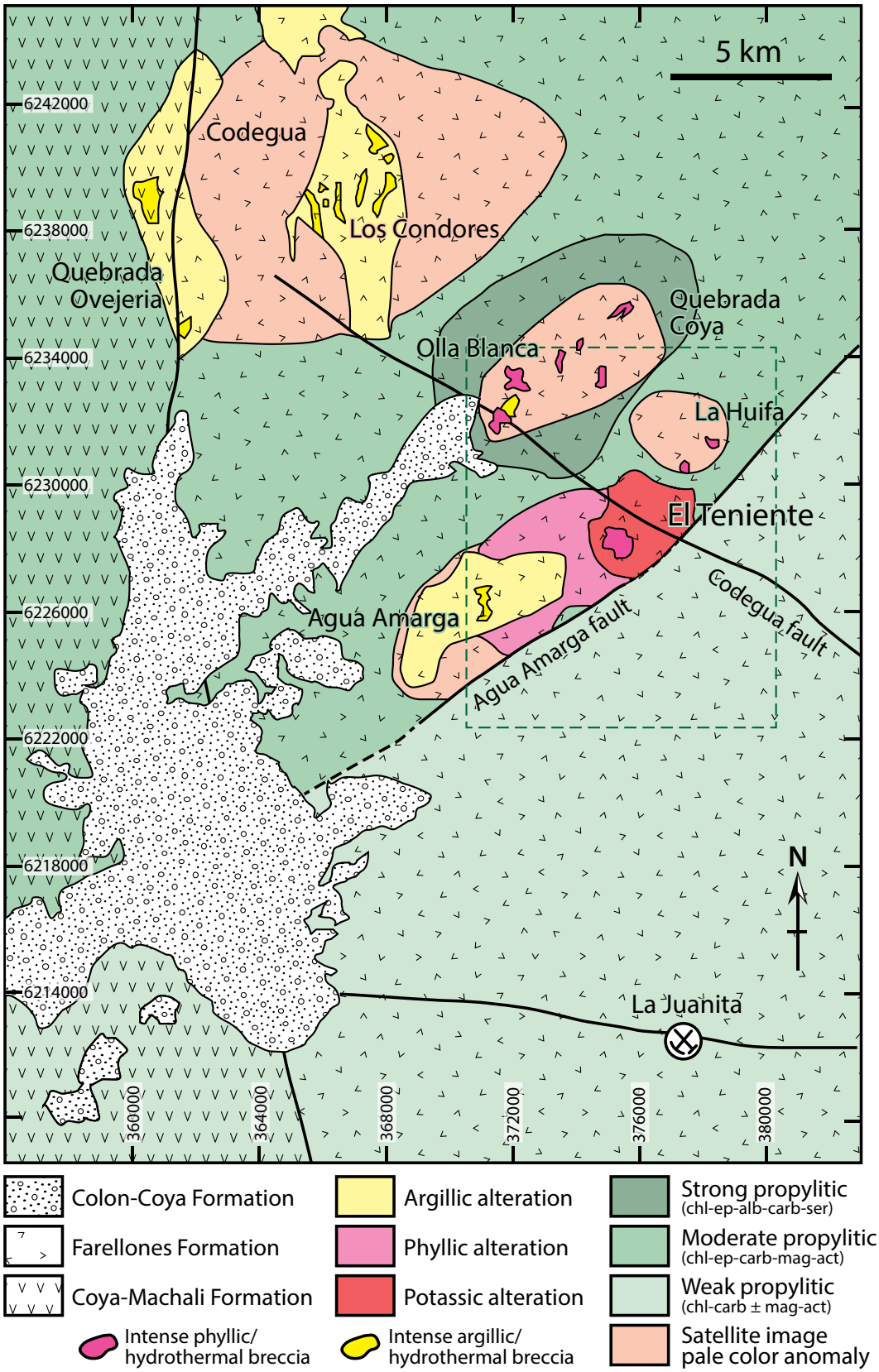

Fig. 1. Simplified geologic map of the El Teniente district, showing distribution of major units, prospects, structures, and alteration domains. Area studied for propylitic mineral chemistry shown in the dashed box (see Fig. 2). Modified from Cannell (2004). Abbreviations: act = actinolite, alb = albite, carb = carbonate, chl = chorite, ep = epidote, mag = magnetite, ser = sericite.

mid-late Miocene Farellones Formation, a >2,500-m-thick sequence of extrusive and intrusive rocks of basaltic to rhyolitic composition (Fig. 1; Skewes et al., 2002; Cannell et al., 2005). In the late Miocene-Pliocene (~6.5–4.5 Ma), the Teniente Mafic Complex was intruded by a series of diorite to granodiorite intrusions associated with multiple igneous and hydrothermal breccia complexes. Mineralization developed in concert with three main magmatic episodes (Spencer et al., 2015), each of which was associated with its own pulse of hydrothermal activity (Vry et al., 2010). Thus, it has been concluded that the deposit represents a nested Cu-Mo porphyry system formed by the emplacement and overprinting of a number of porphyry intrusions that evolved separately in space and over time (Astudillo et al., 2010; Vry et al., 2010; Spencer et al., 2015).

A number of neighboring hydrothermal centers exist in the district, some of which have distinct surface color anomalies due to argillic alteration at surface (Fig. 1). Olla Blanca, ~6 km to the north-northwest of El Teniente, is the oldest (~9 Ma: Maksaev et al., 2004), and mineralization at La Huifa, ~4 km to the north-northeast, has been dated at ~6.6 to 6.5 Ma (Re-Os molybdenite: Pardo, 2015), slightly predating El Teniente at ~6.3 to 4.6 Ma (Spencer et al., 2015).

Propylitic alteration assemblages are widely developed in the El Teniente district (Fig. 1). North of the Agua Amarga fault, pervasive propylitic assemblages occur in the Coya-Machali Formation and, to a lesser extent, in the Farellones Formation. These assemblages are characterized by pervasive chlorite-epidote-calcite ± hematite, and shallowly dipping carbonate veins (±hematite-epidote halos) are common (Cannell, 2004). The similarity between this alteration and the regional lower greenschist metamorphic assemblage that occurs in Mesozoic and Cenozoic rocks has been noted (Morel, 1984). South of the Agua Amarga and Codegua faults (Fig. 1), the intensity of propylitic alteration of the Farellones Formation decreases significantly. Only weak chlorite-carbonate alteration, largely restricted to amygdules in the volcanic units, has been reported (Cannell, 2004).

Propylitic alteration in the vicinity of El Teniente itself forms a distal halo surrounding a core of potassic alteration that comprises intense biotite-magnetite alteration in the Teniente Mafic Complex or K-feldspar within intermediate-felsic intrusive rocks (Cannell et al., 2005; Vry et al., 2010). The transitional potassic-propylitic zone lies within the 0.5% copper grade contour (Fig. 2) and is characterized by a greenish-brown biotite and an increase of chlorite and paragonitic muscovite in the groundmass. Pyrite ± secondary magnetite abundances are locally elevated, and primary igneous magnetite has been replaced by biotite, chlorite, sericite, anhydrite, and rutile (Cannell, 2004). Sulfides and anhydrite are rimmed by, or intergrown with, chlorite and/or sericite (probably paragonitic muscovite), and plagioclase has been weakly to moderately pervasively altered to muscovite and calcite. Epidote-K-feldspar assemblages have been recorded, particularly in deeper parts of the system near the Sewell diorite (Vry et al., 2010).

Outboard of the 0.5% copper contour, the Teniente Mafic Complex contains between 5 and 20% chlorite, occurring mainly as replacements of hornblende and augite phenocrysts. Pyrite is much more abundant relative to chalcopyrite. Pyrite contains pyrrhotite and chalcopyrite inclusions and is rimmed by chlorite. Green, shreddy biotite constitutes up to 25% of the assemblage and decreases in abundance outward. Accessory magnetite, hematite, ilmenite, rutile, anhydrite, quartz, sporadically developed epidote after plagioclase, and rare phengitic muscovite also occur (Cannell, 2004). Propylitic alteration of intrusive rocks (e.g., Sewell diorite, Teniente dacite porphyry) is typified by chlorite and epidote alteration of the ferromagnesian minerals, plus magnetite, hematite, pyrite, sericite, and calcite (Ossandon, 1974). Veins of quartz-epidote (-calcite-chlorite) are variably developed and are cut by quartz-pyrite veins with sericitic alteration halos. Examples of propylitically altered rocks are illustrated in Figure 3.

Previously, this deposit-related alteration was believed to grade out to a district-scale alteration at distances >1 km from the system center (Fig. 1), characterized by replacement of primary mafic minerals and amygdules by chlorite, magnetite, epidote, and hematite, accompanied by weak sericite and albite replacement of plagioclase (Villalobos, 1975; Floody and Huete, 1998).

Methods

One hundred eighty-nine samples of the Farellones Formation (mostly from the Teniente Mafic Complex), comprising largely basaltic to andesitic volcanic rocks and younger intrusions from the El Teniente area, were sampled (Fig. 2).

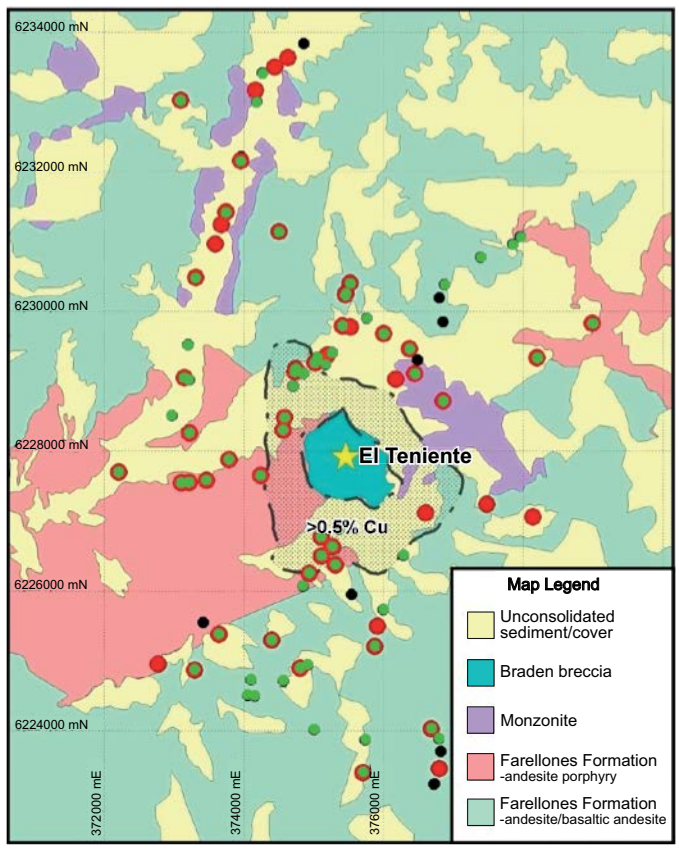

Fig. 2. Simplified geologic map of the study area around El Teniente, showing sample locations for mineral chemistry analysis (drill core and bedrock). Stippled area is the >0.5% Cu ore shell. Black dots = sample not analyzed, green dots = chlorite sample analyzed, red dots = epidote sample analyzed. Note: small areas of outcrop such as in creeks are not visible at this scale. Not shown are additional samples west of easting 370000 that were analyzed for whole-rock geochemistry only. Modified from O. Rivera and M.F. Falcón (unpub. report, 1998).

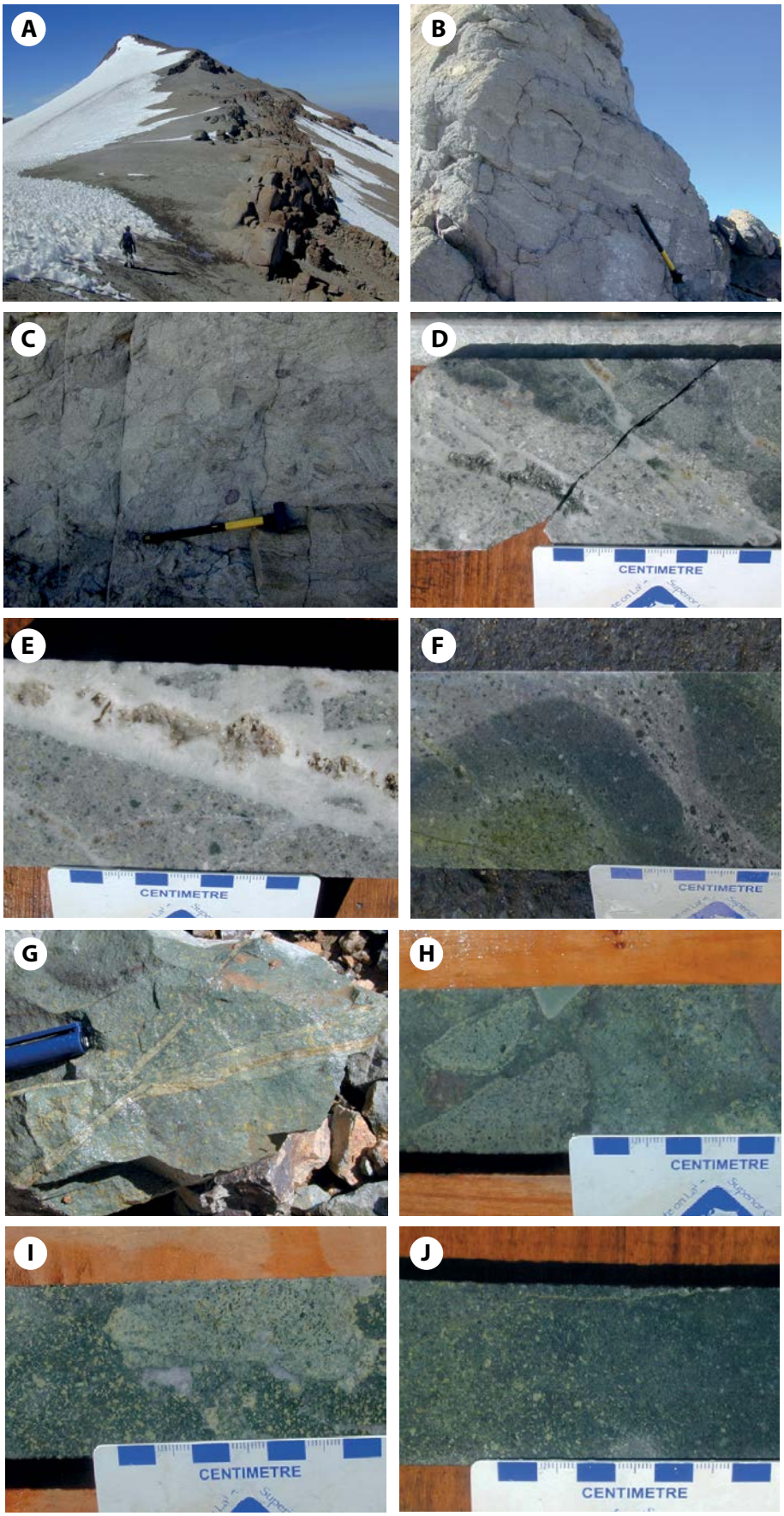

Fig. 3. Photographs illustrating variety of propylitically altered rocks in the El Teniente district. A. Sampling at an elevation of approximately 3,600 m on a ridge approximately 4 km to the south of the deposit center (UTM 0376680 6224030). An intermediate dike (foreground) cuts volcaniclastic rocks of the Farellones Formation. B. Weakly chlorite altered volcaniclastic rock with coarse feldspar phenocrysts, approximately 3.8 km from the deposit center (UTM 0376792 6223890, 3562 m). C. Weak chlorite-hematite alteration in volcanic breccia, approximately 4 km from the deposit center (UTM 0376820 6223710, 3576 m). D. Contact between chlorite-altered volcanic rock of the Farellones Formation and a monzonitic intrusion, approximately 6.0 km north-northwest of the deposit center. Ladder-type quartz(-epidote) veins containing a beige phase (siderite?) cut the contact. Phenocrysts in the monzonite are mostly chlorite altered. DDH ES-236, depth 91.6 m (UTM 373092 6233025, 2737 m). E. Comb-textured quartz vein (elsewhere containing epidote) cutting felsic intrusive rock. Weak epidote replacement of plagioclase phenocrysts and epidote-chlorite replacement of mafic phenocrysts is observed. DDH ES-236, depth 94.9 m (UTM 373092 6233025, 2733 m). F. Rounded clasts of volcanic rock (Farellones Formation?) within monzonite porphyry. Clast cores are rich in epidote, apparently related to the abundant epidote veinlets that cut both lithologies but which develop much broader alteration halos in the mafic rock. Clast margins are chlorite rich, and amphibole phenocrysts in the monzonite have been replaced largely by chlorite. DDH ES-236, depth 342.7 m (UTM 373092 6233025, 2486 m). G. Fine-grained volcanic rock cut by calcite-epidote veins, with pervasive chlorite replacement of groundmass and epidote after plagioclase phenocrysts. A moderate phyllic overprint is present. Near Adit 42, northwest side of Braden breccia pipe, approximately 1 km from deposit center. H. Polymict volcanic breccia displaying variably strong chlorite-hematite alteration in clasts and matrix and epidote replacing plagioclase phenocrysts. DDH ES-234 (UTM 374502 6231145, 3032 m), approximately 3.7 km from the deposit center. I. Intense chloritic alteration of matrix of volcanic breccia with preferential replacement of plagioclase phenocrysts by epidote. Patches and irregular veins of anyhydrite are also observed. DDH ES-234 (UTM 374502 6231145, 2252 m), approximately 3.7 km from the deposit center. J. Gradational change in alteration intensity within Teniente Mafic Complex showing progressive increase in epidote replacement of feldspar phenocrysts and groundmass. DDH ES-234 (UTM 374502 6231145), approximately 3.7 km from the deposit center.

Whole-rock major and trace element data were generated at Acme Analytical Laboratories Ltd. (now Bureau Veritas) in Vancouver, Canada. Samples were jaw crushed to 70% passing 10 mesh (2 mm); a 250-g aliquot was riffle split and pulverized to 95% passing 150 mesh (100 µm) in a mild-steel ring-and-puck mill. A 0.2-g powdered sample was fused in a graphite crucible with 1.5 g of $LiBO_2/LiB_4O_7$ flux at 980°C for 30 min and then dissolved in 5% HNO_3. Major elements were determined using a Jarrel Ash AtomComp Model 975/ Spectro Ciros Vision inductively coupled plasma-emission spectrograph. Trace elements were analyzed using a Perkin-Elmer Elan 6000 or 9000 inductively coupled plasma-mass spectrometer. For major and trace elements, calibration standards, verification standards, and reagent blanks were included in the sample sequence. Reported detection limits are 0.04 wt % for the major elements and 0.5 ppm for the majority of the trace elements, excluding the rare earth elements (REEs; 0.05 ppm). Whole-rock major and trace element data for selected samples are listed in Table 1. Whole-rock major and trace element data for all samples are listed in Appendix Table A1.

One hundred thirty-five representative samples containing minerals of interest were prepared as 25-mm polished resin mounts for scanning electron microscopy (SEM) backscattered electron imaging of mineral relationships, electron microprobe-wavelength dispersive spectrometry analysis (EMP-WDS), and laser ablation-inductively coupled plasma-mass spectrometry (LA-ICP-MS).

Major and minor elements in individual chlorite and epidote grains were determined using a Cameca SX100 electron microprobe housed in the Central Science Laboratories at the University of Tasmania. Full results from 755 analyses of chlorite and 316 from epidote are reported in Appendix Tables A2 and A3, respectively. Major, minor, and trace elements in the same grains were measured using a New Wave 193-nm solid-state laser coupled to an Agilent 7500cs quadrupole mass spectrometer, located in the School of Physical Sciences, Discipline of Earth Sciences, University of Tasmania. Typically, five to 10 spot analyses were acquired from each sample, from within three to five separate mineral grains. For each analysis, 30 s of background signal was acquired prior to 60 s of mineral ablation. Ablation was performed in an atmosphere of pure He (~0.7 L/min) using spots ranging in diameter from 30 to 55 µm with a laser repetition rate of 10 Hz. Laser beam fluence at the sample was ~3 J/cm^2.

For epidote, a total of 37 elements were determined on each spot by analysis of the following isotopes: ^{23}Na, ^{24}Mg, ^{27}Al, ^{29}Si, ^{39}K, ^{43}Ca, ^{47}Ti, ^{51}V, ^{55}Mn, ^{57}Fe, ^{59}Co, ^{65}Cu, ^{66}Zn, ^{69}Ga, ^{75}As, ^{88}Sr, ^{89}Y, ^{90}Zr, ^{95}Mo, ^{107}Ag, ^{118}Sn, ^{121}Sb, ^{137}Ba, ^{139}La, ^{140}Ce, ^{153}Eu, ^{157}Gd, ^{172}Yb, ^{175}Lu, ^{178}Hf, ^{181}Ta, ^{197}Au, ^{205}Tl, ^{208}Pb, ^{209}Bi, ^{232}Th, and ^{238}U. Acquisition time for each mass was set to 0.02 s, with the exceptions of Na, Al, and Si (0.005), Mg, K, Ca, Ba, La, Ce, and U (0.01), and Mo, Ag, Sn, and Au (0.03). For chlorite, 32 elements were determined on each spot by analysis of ^{7}Li, ^{9}Be, ^{11}B, ^{23}Na, ^{24}Mg, ^{27}Al, ^{29}Si, ^{39}K, ^{43}Ca, ^{47}Ti, ^{51}V, ^{53}Cr, ^{55}Mn, ^{57}Fe, ^{59}Co, ^{60}Ni, ^{65}Cu, ^{66}Zn, ^{69}Ga, ^{75}As, ^{88}Sr, ^{89}Y, ^{90}Zr, ^{107}Ag, ^{118}Sn, ^{121}Sb, ^{137}Ba, ^{139}La, ^{140}Ce, ^{208}Pb, ^{209}Bi, and ^{238}U. Acquisition time for each mass was set to 0.02 s, with the exceptions of Na, Mg, and Si (0.005), Al, K, Ca, Mn, Fe, and U (0.01), and Co, Cu, As, Ag, Sn, Sb, and Bi (0.03).

No corrections for interfering molecular or isobaric species were required due to the selection of appropriate analytical isotopes and the minimization of molecular species formation. Signal processing was done using an in-house Excel macro and the ExLAM Excel VBA application (Zacharias and Wilkinson, 2007). In total, 641 LA-ICP-MS spot analyses of chlorite (from 115 samples) and 592 of epidote (from 103 samples) meeting quality control criteria (i.e., avoiding contamination from mineral inclusions) were obtained.

Aluminum and calcium concentrations determined by microprobe were used as the internal standards for reduction of chlorite and epidote LA-ICP-MS data, respectively. NIST612 standard reference material was used for external calibration of the LA-ICP-MS results according to standard practice. Full LA-ICP-MS results are reported in Appendix Table A4.

Results

Whole-rock geochemistry

Key pathfinder elements were grouped into eight percentile bins (1, 5, 10, 25, 75, 90, 95, and 99%) and plotted in plan view to define the conventional geochemical footprint of the deposit. Anomalous Cu above a background population (>230 ppm), defined by a natural break in the cumulative probability curve, is observed in a fairly coherent anomaly surrounding the deposit, extending up to 1 km from the edge of the 0.5 wt % Cu contour. Some additional anomalous samples are observed between El Teniente and La Huifa but none in the vicinity of Olla Blanca (Fig. 4A).

Anomalous Mo (>2.1 ppm) is somewhat erratically distributed across the district. Consistently elevated values are observed close to El Teniente but are very proximal, occurring within the 0.5 wt % Cu contour. As with Cu, there are elevated values in the vicinity of La Huifa, but for Mo there is a marked gap between the two systems, with background values in between (Fig. 4B). Olla Blanca samples are not anomalous in Mo.

Anomalous Mn (>1,280 ppm) is more broadly distributed than the principal ore metals and appears to form a crude halo around the 0.5 wt % Cu ore shell, with maximum values between 0.5 and 1 km from its edge and lower concentrations within it (Fig. 4C). Neither La Huifa nor Olla Blanca show Mn anomalism.

The Zn anomaly around El Teniente (>170 ppm) is slightly better developed than Mn, but they are comparable in form (Fig. 4D). Their covariance is confirmed by a robust linear regression that yields an R^2 value of 0.74. One point to note for both Mn and Zn is that the results for neighboring samples, or for those from the same drill hole, can be very variable, indicating a nugget effect on the hand-sample scale. As with Mn, neither La Huifa nor Olla Blanca show enrichment in Zn.

Lead shows a similar pattern to Cu with a slight asymmetry to the north and west but has a greater extent of anomalism (above 12.9 ppm) up to 2.5 km from the edge of the 0.5 wt % Cu contour (Fig. 4G). There is arguably a small separation between El Teniente and La Huifa, with the latter system showing some apparently associated anomalous samples to the south and east, very much like Cu and Mo. Olla Blanca is not anomalous in whole-rock Pb (Fig. 4G).

It is difficult to define the background level for As in the district, because ~90% of the data fall above the upper crust-

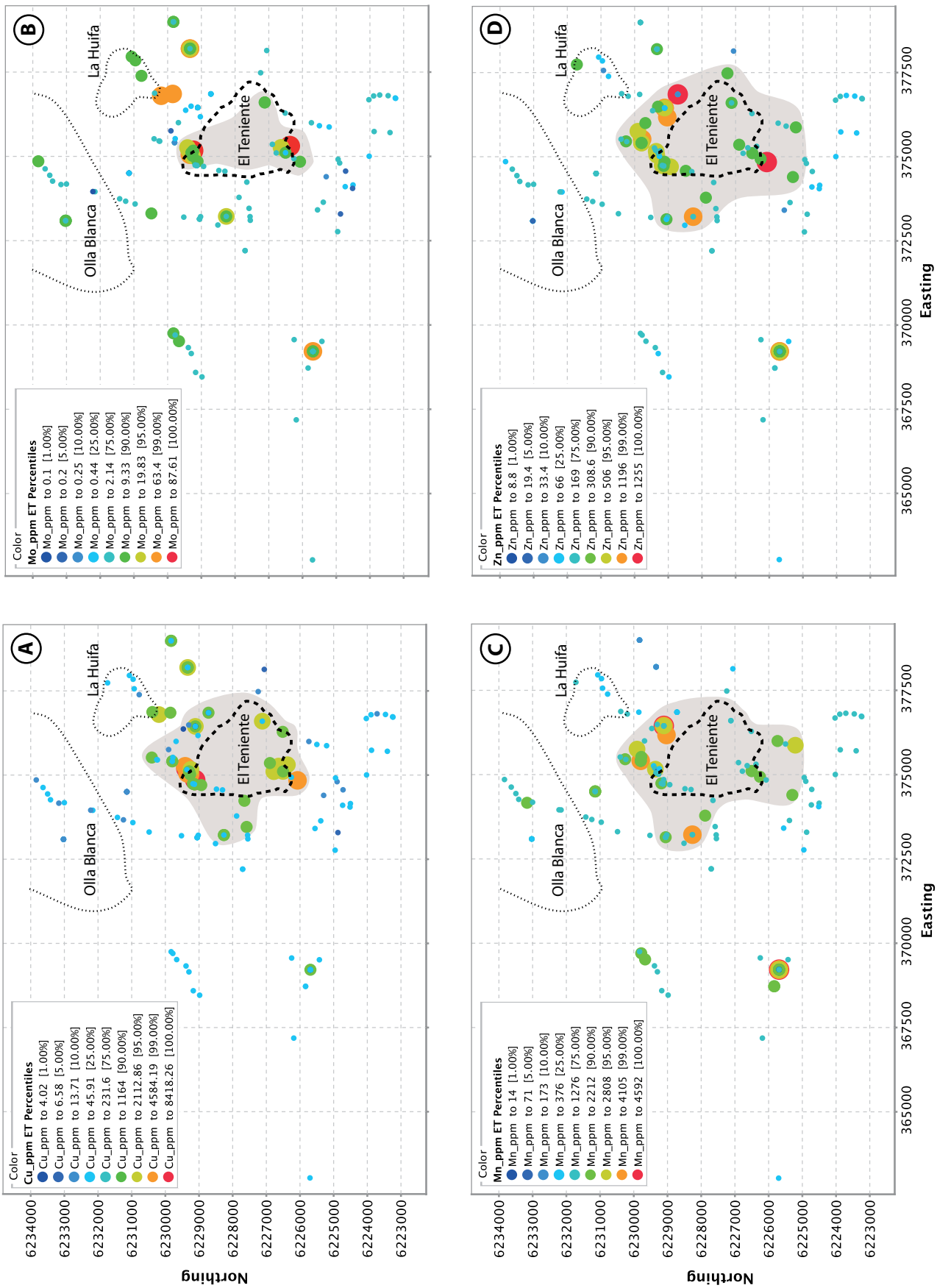

Fig. 4. Footprint of El Teniente as defined by whole-rock geochemistry. A-D. A. Cu using percentile bins at 1, 5, 10, 25, 75, 90, 95, 99, and 100%. B. Mo (same percentiles). C. Mn (same percentiles). D. Zn (same percentiles).

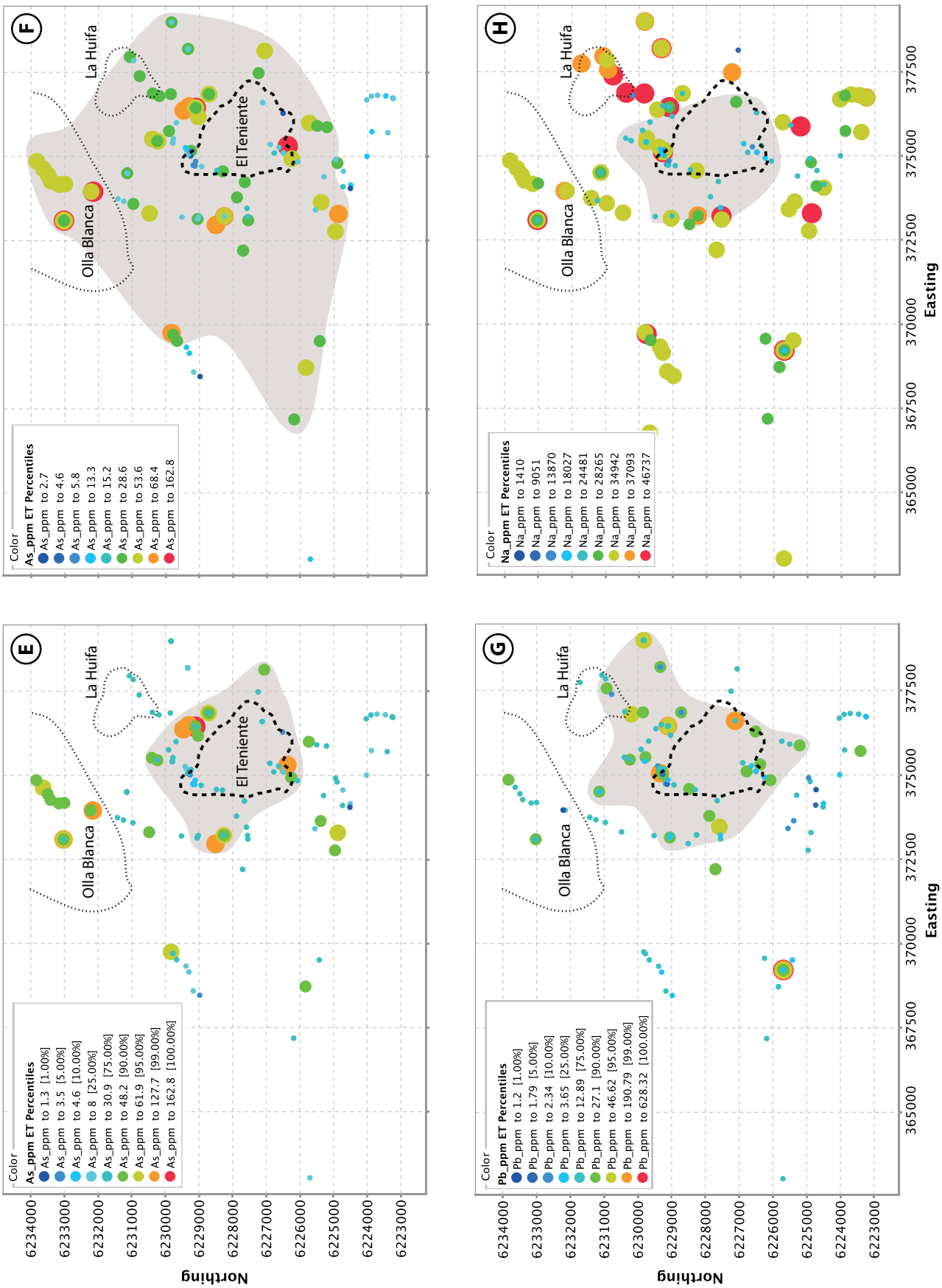

Fig. 4. (*Cont.*) Footprint of El Teniente as defined by whole-rock geochemistry. E-H. E. As (same percentiles). F. As using natural breaks in the data. G. Pb (same percentiles). H. Na (using natural breaks in the data). Inferred extent of coherent anomaly associated with El Teniente is shown in the gray field. Note: Na is a low-proximal anomaly. Thick dashed line indicates El Teniente 0.5% Cu grade contour. Northing grid has 1-km spacing.

Table 1. Mean Compositions of Selected, Relatively Unaltered Lithologies from the Farellones Formation and Younger Intrusive Rocks in the El Teniente Area

	Rhyolite	Dacite	Andesite	Basalt	Grano-diorite	Quartz monzo-nite	Monzo-nite	Diorite
N	1	2	23	1	6	2	2	8
SiO_2	68.72	67.10	54.60	49.25	64.95	67.94	59.79	58.89
Al_2O_3	17.57	16.08	17.64	17.68	16.62	14.75	17.15	17.47
Fe_2O_3	1.62	3.50	8.70	11.87	4.28	3.55	6.46	6.74
MgO	0.65	1.14	3.92	6.03	1.60	1.16	2.24	2.46
CaO	0.44	2.86	5.99	5.52	3.43	2.45	5.45	5.40
Na_2O	4.54	4.71	3.79	2.19	4.80	3.39	4.03	4.00
K_2O	4.30	2.86	1.36	0.73	2.57	4.95	2.26	2.13
TiO_2	0.38	0.38	0.91	0.95	0.50	0.42	0.73	0.75
P_2O_5	0.18	0.12	0.24	0.14	0.15	0.10	0.20	0.22
MnO	<0.01	0.05	0.20	0.27	0.04	0.09	0.07	0.12
Cr_2O_3	<0.002	0.003	0.008	0.020	0.004	<0.002	0.004	0.003
LOI	1.30	1.00	2.39	5.00	0.87	1.10	1.45	1.63
Σ C	<0.01	0.04	0.20	0.26	n.d.	n.d.	n.d.	0.02
Σ S	0.23	0.07	0.52	1.04	n.d.	n.d.	n.d.	0.36
Ag	0.16	0.10	0.10	0.30	0.03	0.07	0.03	0.05
As	3.4	15.5	33.8	7.0	13.7	33.9	29.6	14.4
Au	1.4	3.3	1.5	1.5	0.8	0.5	0.7	3.4
B	10.0	10.5	4.5	7.0	4.5	3.5	6.5	3.1
Ba	742	604	281	59.0	559	572	460	435
Be	0.20	0.20	0.25	0.20	0.10	0.25	0.15	0.12
Bi	0.23	0.22	0.40	1.16	0.19	0.03	0.03	0.03
Cd	0.42	0.11	0.12	0.02	0.11	0.07	0.05	0.09
Ce	16.2	24.8	31.0	13.1	33.3	40.9	36.2	39.6
Co	0.60	6.9	23.0	42.4	9.3	6.2	14.1	14.7
Cr	1.8	10.9	34.2	106	16.9	9.0	16.4	18.1
Cs	2.7	3.7	1.9	11.5	1.0	0.5	0.6	0.6
Cu	615	182	161	474	154	24.2	79.0	123
Dy	0.64	0.95	3.36	2.32	1.40	2.75	2.77	2.47
Er	0.49	0.55	1.86	1.33	0.71	1.60	1.47	1.33
Eu	0.45	0.55	1.14	0.88	0.78	0.67	1.13	1.05
Ga	20.7	19.0	19.1	20.7	19.4	18.0	20.1	20.0
Gd	1.08	1.45	3.90	2.39	2.07	3.10	3.66	3.36
Ge	<0.1	<0.1	0.15	0.20	<0.1	0.20	0.10	0.10
Hf	2.70	3.45	3.49	1.60	3.73	6.90	4.50	4.34
Hg	17.0	6.0	5.20	9.0	<0.01	<0.01	<0.01	15.0
Ho	0.11	0.18	0.66	0.47	0.26	0.54	0.54	0.48
In	<0.02	0.02	0.05	0.20	0.02	<0.02	<0.02	0.03
La	7.0	11.6	13.6	5.0	15.6	18.3	18.3	17.6
Li	1.70	4.65	9.51	21.8	3.45	5.40	4.80	6.04
Lu	0.03	0.06	0.26	0.20	0.11	0.27	0.23	0.19
Mn	18.0	301	1,100	1,970	174	469	231	480
Mo	6.76	5.65	1.40	2.28	2.38	3.39	1.46	1.54
Nb	2.60	3.05	3.53	1.70	3.25	6.40	4.55	4.68
Nd	7.10	10.45	18.70	8.40	17.28	19.25	22.00	21.28
Ni	0.80	6.05	20.9	56.2	8.90	5.70	9.70	13.5
Pb	14.2	6.3	8.5	2.7	14.6	9.8	3.5	10.1
Pd	<10	<10	<10	<10	<10	<10	<10	<10
Pr	1.92	2.89	4.28	1.92	4.31	5.15	5.32	5.15
Pt	<2	<2	4	3	<2	<2	<2	3
Rb	99.3	75.7	42.1	36.6	77.1	164	67.0	67.5
Re	3.0	4.0	13	14	1.5	4.0	<1	4.0
Sb	0.07	0.39	1.00	0.58	0.43	1.62	0.42	0.37
Sc	3.00	4.50	18.9	26.0	6.00	6.00	10.5	11.1
Se	0.20	0.15	0.47	0.30	0.14	0.25	0.25	0.27
Sm	1.31	1.78	4.19	2.29	2.97	3.86	4.38	4.21
Sn	2	<1	1	3	n.d.	n.d.	n.d.	2
Sr	280	547	524	375	643	326	591	580
Ta	0.20	0.30	0.23	<0.1	0.27	0.55	0.30	0.30
Tb	0.11	0.18	0.62	0.40	0.28	0.51	0.55	0.50
Te	0.04	0.04	0.17	0.26	0.03	0.05	0.03	0.07
Th	4.00	8.30	4.89	1.00	8.83	24.7	8.20	7.53
Tl	0.05	0.06	0.28	0.05	0.04	0.07	<0.02	0.04
Tm	0.03	0.05	0.29	0.20	0.11	0.27	0.23	0.21
U	1.70	2.70	1.47	0.50	2.52	7.25	2.50	2.18
V	43.0	51.5	199	247	88.3	61.0	141	139
W	24.6	3.15	1.86	4.60	2.25	1.00	0.90	1.55
Y	5.00	5.45	18.75	12.60	7.78	17.15	16.35	14.13
Yb	0.39	0.52	1.77	1.24	0.73	1.73	1.44	1.30
Zn	146	48.4	124	305	101	52.0	26.0	73.7
Zr	101	109	117	54.7	123	208	150	147

The limit of detection where concentrations could not be determined is denoted by "<xx"; all major oxides, total C, S, and loss on ignition (LOI) in wt %; trace elements in ppm apart from Au, Pd, Pt, and Re, which are in ppb; *N* = number of analyses included in average; n.d. = not determined; representative samples of different rock types were used, screened for alteration effects, such as elevated LOI (>2.5 wt %) or ore metals, and excluding outlying compositions for a given rock type; full data set reported in Appendix Table A1

al average of 4.8 ppm (Rudnick and Gao, 2003) suggesting a very broad enrichment that may be partly premineralization in origin based on the elevated values in ostensibly unaltered samples (Table 1). Using the same percentile bins as above, a relatively weak footprint is defined (Fig. 4E) with elevated values (>31 ppm) occurring in a halo around El Teniente at a distance of 0.5 to 1 km from the edge of the ore shell. La Huifa shows no As anomalism; conversely, Olla Blanca has markedly elevated As concentrations in a number of samples. Alternatively, if a complex set of natural breaks in the data are considered, values above a putative background of 15 ppm define a very broad, asymmetric footprint that extends up to 7.5 km from the edge of the 0.5 wt % Cu contour in the northwest quadrant and to the limit of sampling in most areas (Fig. 4F). The most clearly defined limit is at around the 6225000 northing, to the south of which only low As concentrations are observed.

Several elements show proximal low patterns that can be discerned in whole-rock data, most notably Na and Sr. For Na, based on natural breaks in the data, anomalously low concentrations below 2.45 wt % fairly effectively define a proximal footprint broadly centered on the orebody but extending up to 1.5 km from the 0.5 wt % Cu contour to the north and west (Fig. 4H).

In all cases, the whole-rock anomalies defined are imperfect in the sense that the samples with elevated values in the inferred footprints are frequently accompanied by neighboring samples with background-level concentrations. This implies heterogeneity in pathfinder metal distribution that may reflect control by somewhat erratically distributed, perhaps structurally controlled, sulfides.

Chlorite major element chemistry and thermometry

Major element compositions of chlorite correspond to the clinochlore-chamosite solid solution with a wide range in Fe (8.4–26.6 wt %) and Mg (5.1–15.2 wt %) content determined by microprobe, excluding one very Fe rich sample (Fig. 5). Median Al and Si contents determined by microprobe were

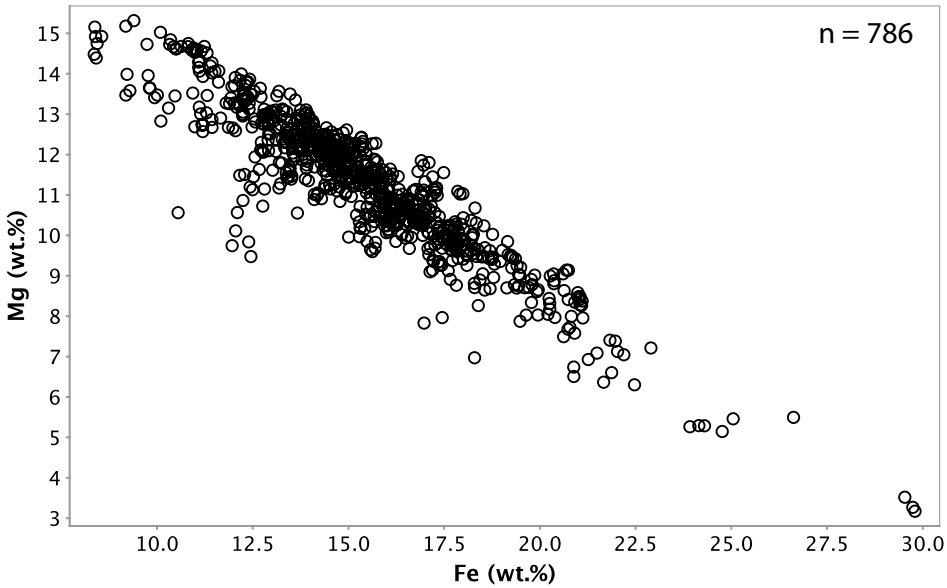

Fig. 5. Iron and magnesium content of chlorites, determined by electron microprobe.

10.2 and 13.2 wt %, respectively. Manganese contents determined by microprobe ranged up to 6.1 wt %, but the vast majority were <2 wt % Mn.

Chlorite crystallization temperatures were calculated from microprobe data using the thermodynamic model of Walshe (1986). Sample average temperatures derived from this approach are in the range 113° to 356°C with an overall mean of 241°C (App. Table A2). Gridding the data shows that the temperatures define a clear thermal anomaly associated with the ore deposit and with a subsidiary anomaly in the vicinity of La Huifa (Fig. 6).

Although chlorite thermometry is complex, with the temperature-related Al^{IV} Tschermak substitution $(Si^{4+})^{IV}(Mg^{2+})^{VI} = (Al^{3+})^{IV}(Al^{3+})^{VI}$ also related to $a_{H_4SiO_4}$, $a_{Al^{3+}}/(a_{H^+})^3$, $a_{Fe^{2+}}/(a_{H^+})^2$, $a_{Mg^{2+}}/(a_{H^+})^2$, and a_{H_2O} (de Caritat et al., 1993), we can argue that, at least in a semiquantitative sense, the thermometry results are robust. This is because silica activity is likely to be buffered at quartz saturation in propylitic fluids, and pH and Al activity will be buffered by the aluminosilicate assemblage in the host rocks at the relatively low water/rock ratios expected in the propylitic domain. We also know from fluid inclusion data that propylitic fluids at El Teniente are water rich (Wilkinson et al., 2019) and that a_{CO_2} must be low for epidote to be stable (Bird and Spieler, 2004) so that we can assume a_{H_2O} ~1.0. The principal remaining variables that may have some effect are the activities of Mg^{2+} and Fe^{2+} in the fluid. These may be controlled, at least in part, by the composition of the host rock, with more mafic compositions yielding higher Fe chlorites (see below). However, the relatively uniform bulk composition of most of the host rocks (104 out of 189 are basaltic andesite-andesite based on silica content; App. Table A1) means that any effect will be limited. Finally, we see an excellent negative correlation between chlorite Si^{IV} and calculated temperature (robust regression $R^2 = 0.77$), consistent with the Tschermak exchange and as observed in geothermal data sets (e.g., Cathelineau, 1988). Thus, although the absolute temperatures reported (App. Table A2) should be treated with caution, we are confident of the thermal footprint defined.

Chlorite trace element chemistry

Manganese, Ca, Zn, V, K, Co, Ni, Ti, Li, Na, and Ga were the most common trace elements (generally 10s to 100s of ppm) determined in chlorite in decreasing order of abundance (Fig. 7). The presence of Mn, Zn, Ni, and Li is not unexpected, as they represent partial solid solution toward pennantite, baileychlore, nimite, and cookeite end members, respectively, of the chlorite series. Vanadium^{3+} may substitute for Al^{3+} in octahedral coordination, analogous to Cr^{3+} in kämmererite, and Co^{2+} has similar ionic radius to Fe^{2+} and Ni^{2+}, so it is likely to occur in similar octahedral coordination. Titanium^{4+} is also known to substitute into octahedral sites.

The trace components Cu, Sr, As, Ba, Sn, Pb, Y, Zr, Ce, and La, mostly present at concentrations of tens of parts per million or less, were also detected in more than two-thirds of the analyses (Fig. 7) and are assumed to be substituted into chlorite structural sites on the basis of smooth signals in LA-ICP-MS analyses. Copper shows a particularly wide range and a positive skew, which may reflect the unrecognized incorporation of sulfide nanoinclusions in some analyses; however, many high signals are extremely homogeneous and consistent from grain to grain in a given sample so that, for the most part, high-Cu chlorites probably do reflect structural substitution. Close correspondence between the ionic radius of Cu^+ and Li^+ supports their potential substitution in the same sites. Less consistently detected were Cr, B, Mo, Sb, Ag, Bi, and U, which may reflect their presence in mineral nanoinclusions. The lowest limits of detection for some of the heavier elements were ~4 ppb.

Protolith controls of chlorite chemistry

An important factor to consider when interpreting mineral chemistry data is the possible control by the protolith (bulk-rock chemistry) on major and trace element compositions.

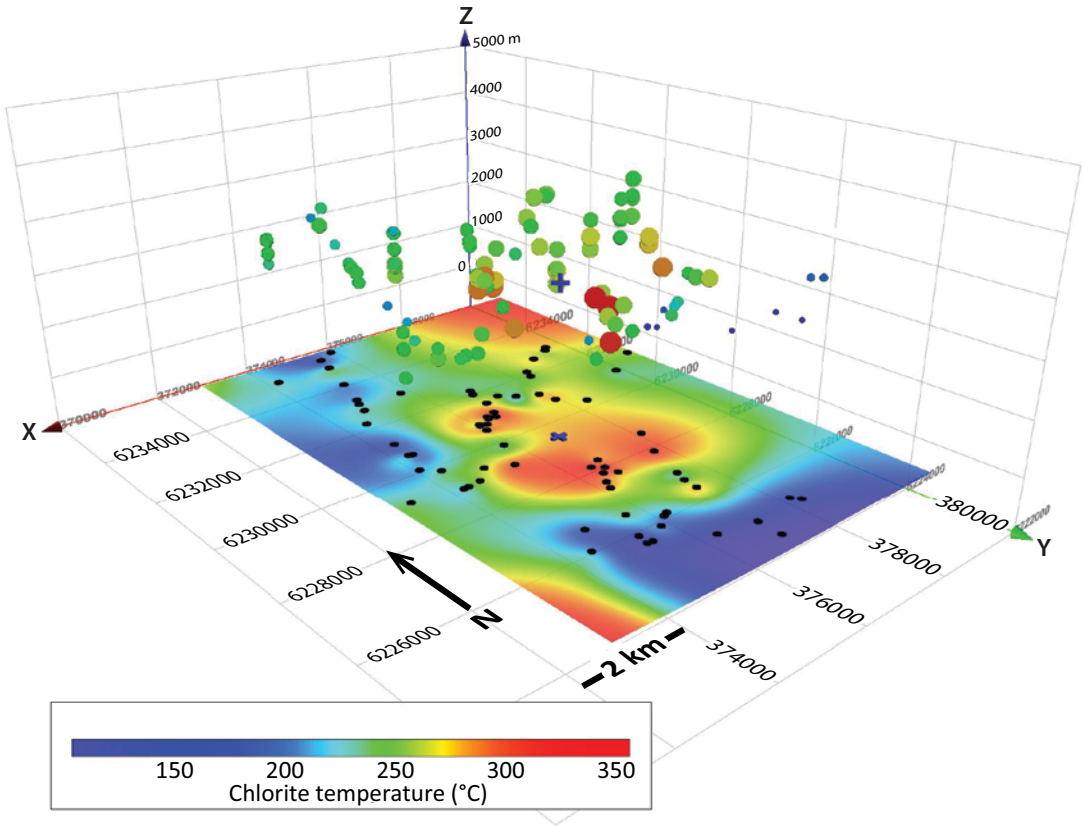

Fig. 6. Chlorite geothermometry temperatures at El Teniente shown as sample averages, plotted in 3-D coordinates (no vertical exaggeration) and projected onto plan view. Warm symbol colors = higher temperatures. Cross shows the location of the inferred center of the ore deposit. Note steep thermal gradients to the south of the deposit, broadly coincident with the position of the Teniente fault zone and the southern boundary of the Sewell diorite, parallel to the Agua Amarga fault. The thermal anomaly to the northeast corresponds to the position of the La Huifa deposit (11.1 Mt at 1% Cu and 0.039% Mo; Floody and Huete, 1998).

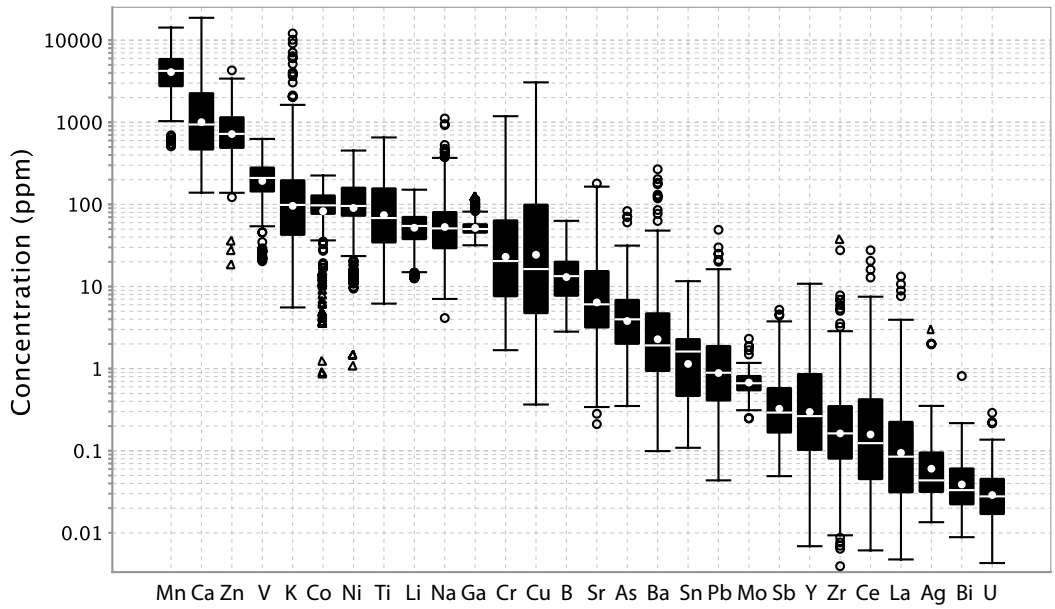

Fig. 7. Summary of compositional ranges for minor and trace elements in chlorite from El Teniente. Dot represents mean value; horizontal line represents median; box represents 25th to 75th percentiles; whiskers represent maximum and minimum excluding outliers; circles represent outliers (>1.5× interquartile range from the box); triangles represent far outliers (>3× interquartile range from the box).

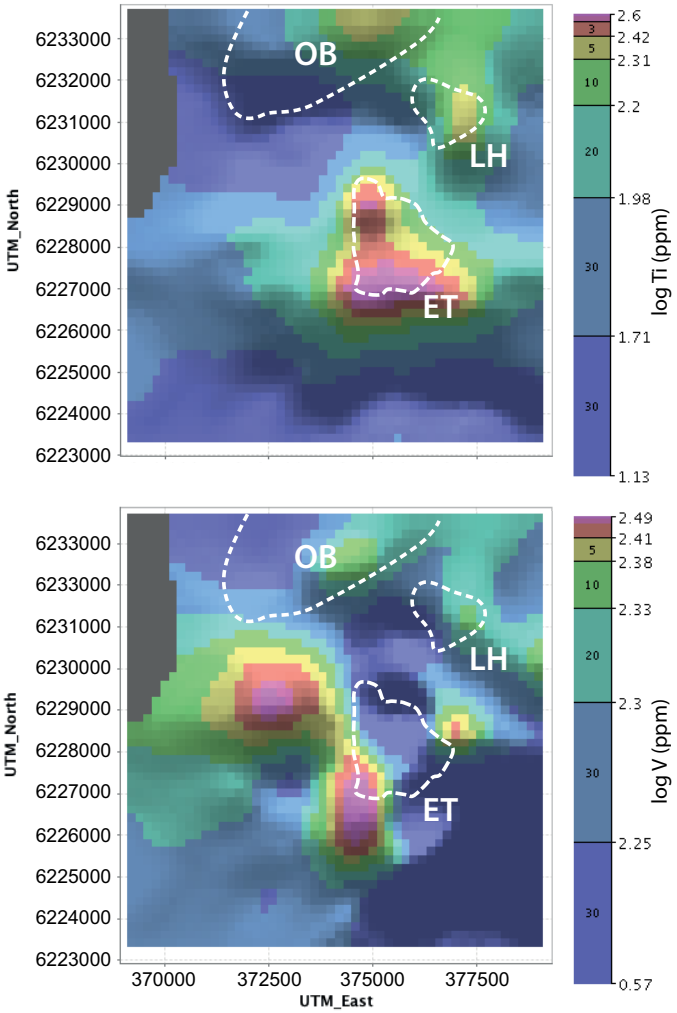

Fig. 8. Gridded chlorite compositional data (log of sample average, cell size 200 m, minimum smoothing distance four cells) for trace elements showing proximal highs. The Ti anomaly coincides with the ore shell; the V anomaly forms a proximal shoulder with apparent asymmetry toward the west. The El Teniente (ET) dashed line is the 0.5 wt % Cu shell; other dashed lines delineate the appromiate extent of the other alteration systems (LH = La Huifa, OB = Olla Blanca). Color scales show range of values for each element, in percentile bands.

However, it is often difficult to separate protolith from spatial controls, particularly in systems where lithologies are heterogeneously distributed. This is the case at El Teniente, where more felsic intrusive rocks predominate in the central parts of the system (Fig. 1).

In order to evaluate protolith effects, the data reported here were divided into groups based on host rock lithology (see App. Table A1). This approach shows that there is a likely influence on Fe and Mg incorporation in chlorite (App. Fig. A1A), with more mafic rocks hosting more Fe-rich chlorite. Because of the strong coupled substitution with Mg, this also leads to lower Mg in chlorite in these samples, even though these rocks are still relatively Mg rich. Silicon and Al show no resolvable protolith control. Most trace elements in chlorite show no correlation with lithology, with the exception of some of those shown in Appendix Figure A1B. Arsenic and Sb tend toward higher concentrations in the more mafic rocks, but this is probably related to their tendency to be located in more distal positions. This behavior is more clearly illustrated by K and Zr, which are rich in the more felsic rocks but are generally elevated in chlorite from the more mafic lithologies, probably for the same reason (enriched in more distal propylitic samples). Nickel and Cr can display protolith effects, but there is no evidence of this in the El Teniente data.

Chlorite spatial variations

The major elements do not show very systematic spatial patterns. Iron and Mg are influenced by protolith as noted above, which obscures spatial patterns, but there is possibly a high shoulder in the Fe data located outside the ore shell (see App. Fig. A2), similar to what was observed at Batu Hijau (Wilkinson et al., 2015). Aluminum perhaps displays a tendency toward higher concentrations in proximal positions (indirectly reflecting a higher formation temperature) and Si tends to be low in proximal samples (see App. Fig. A2).

Clear spatial zonation patterns are observed for a number of trace elements in chlorite, including a proximal high for Ti, with additional small anomalies spatially associated with La Huifa and Olla Blanca (Fig. 8). Vanadium shows a proximal shoulder, with lows in the core of the deposit and a maximum around the margin of the copper ore shell (Fig. 8). There are proximal lows for Li, As, Co, Sr, Ca, La, and Y, and these elements increase distally (Fig. 9). Similar patterns of trace element variation in chlorite have been noted at Batu Hijau and Resolution (Wilkinson et al., 2015; Cooke et al., 2020).

Epidote major element chemistry

Major element compositions of the analyzed epidote correspond to true epidote, with a systematic inverse correlation between Fe and Al representing compositions along the epidote-clinozoisite solid solution (Fig. 10). Iron concentrations were mostly in the range 6.5 to 13.1 wt % (median 10.0 wt %) and Al in the range 10 to 15 wt % (median 13.3 wt %). The median Ca and Si contents were 16.5 and 17.3 wt %, respectively. Manganese contents determined by microprobe ranged up to 2.4 wt %, but the vast majority were <1 wt %.

Epidote trace element chemistry

Manganese, Sr, Mg, Ti, V, and As were the most common trace components in epidote (in decreasing order of abundance), with concentrations mostly exceeding 100 ppm (Fig. 11). Substitution of Mn, Sr, and V represent the solid-solution series toward piemontite, epidote-Sr, and mukhinite, respectively. Titanium and Mg were also frequently detected by microprobe (also see Cooke et al., 2014b; Baker et al., 2020), which, with its much better spatial resolution (~5 vs. 40 µm), is more likely to avoid unrecognized mineral contaminants so that these elements are likely to be structurally bound. Zonation in LA-ICP-MS maps (Cooke et al., 2014b, 2020) shows that As (and Sb) is also incorporated into the epidote structure, probably as As^{3+} in the M site.

Trace components Ga, Pb, Na, Sb, Zn, Ce, La, Y, Zr, Sn, Ba, Eu, U, Yb, Th, and Lu were determined in the 0.01- to 200-ppm range in more than two-thirds of the analyses (Fig. 11) and are also believed to be substituted into the

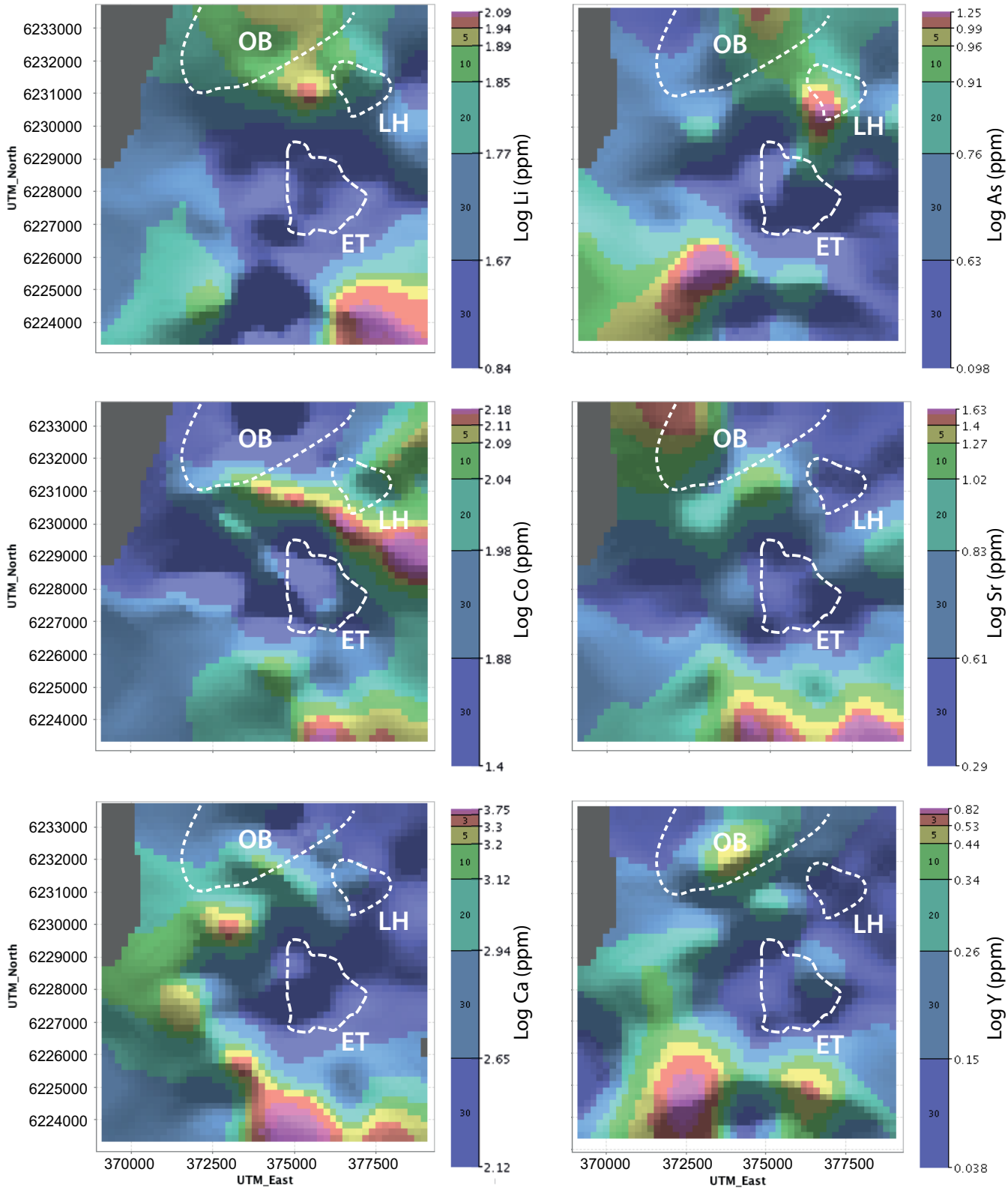

Fig. 9. Gridded chlorite compositional data (log of sample average, cell size 200 m, minimum smoothing distance four cells) for trace elements showing proximal lows. Note the apparent slight northwest-westward offset between some of the chlorite anomalies and the location of the orebody at depth. The El Teniente (ET) dashed line is the 0.5 wt % Cu shell; other dashed lines delineate the appromiate extent of the other alteration systems (LH = La Huifa, OB = Olla Blanca). Color scales show range of values for each element, in percentile bands.

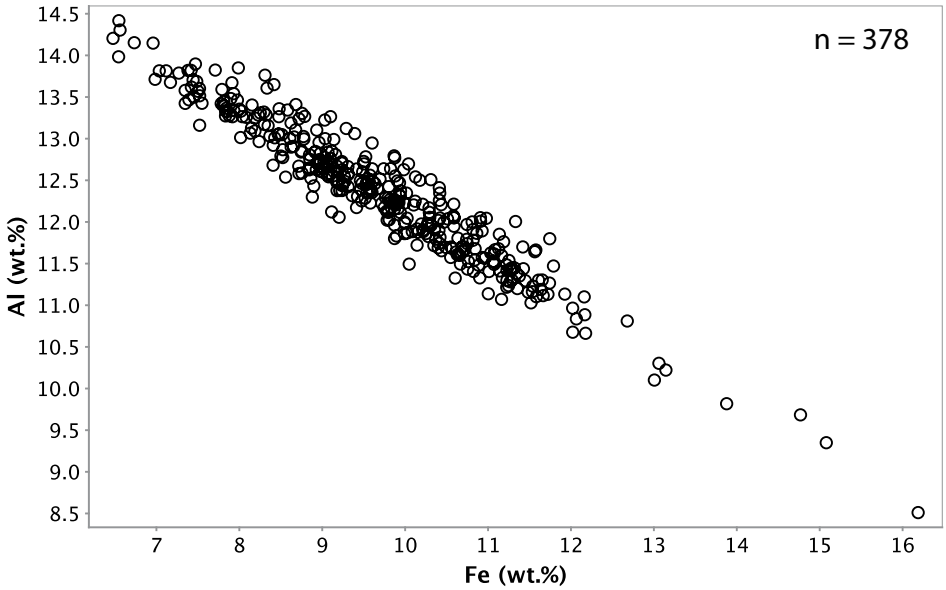

Fig. 10. Iron and aluminum content of epidotes, determined by electron microprobe.

epidote structure. The REEs are common, and sometimes major, structural components in the epidote group, substituting into the trivalent M site. Potassium, Cu, Co, Mo, Bi, Hf, Au, Tl, and Ta were also detected but less consistently and may be present in mineral nanoinclusions that were too small to be discriminated as separate phases during laser signal processing. For K (Na), Cu, and Bi, this interpretation is supported by the marked positive skew observed in the results, with markedly higher mean than median concentrations (Fig. 11). The particularly wide ranges observed for Sb, the REE-Y, Th, and U is due to compositional zoning that is frequently observed in SEM-backscattered imaging and in LA-ICP-MS maps (Cooke et al. 2014b, 2020).

Protolith controls of epidote chemistry

For epidote, there are no discernible effects of protolith on epidote major element chemistry (App. Fig. A3A). For the trace elements, the vast majority show no discernible relationship to lithology, perhaps with the exception of Ba, Pb, Sr, and Zr (App. Fig. A3B). Barium appears to be slightly richer in basalts relative to andesites and monzonites; however, the granodiorite-hosted samples tend to be slightly enriched.

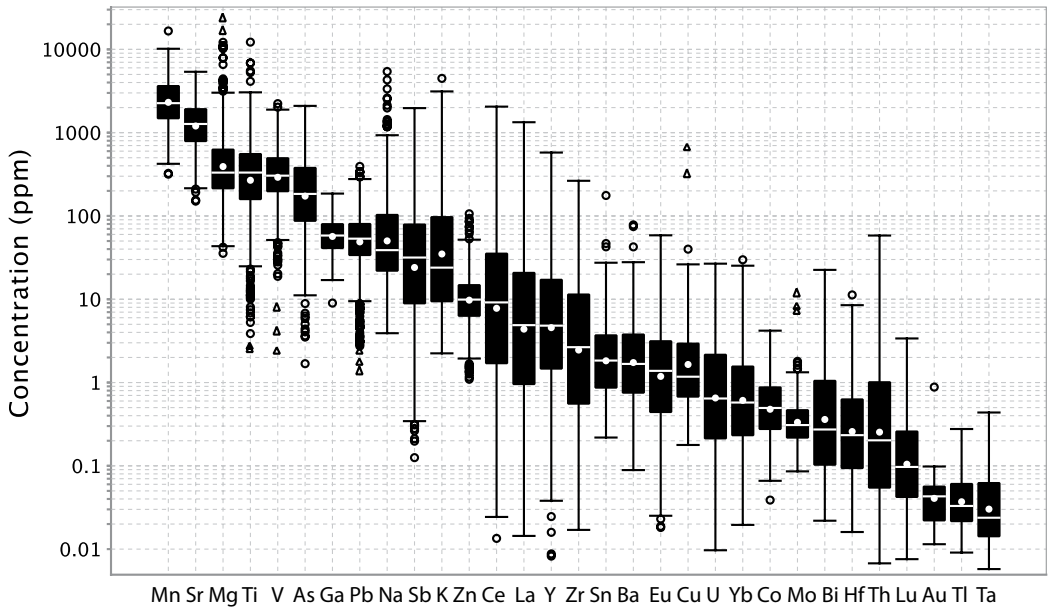

Fig. 11. Summary of compositional ranges for minor and trace elements in epidote from El Teniente. Dot represents mean value; horizontal line represents median; box represents 25th to 75th percentiles, whiskers represent maximum and minimum excluding outliers; circles represent ouliers (>1.5× interquartile range from the box); triangles represent far outliers (>3× interquartile range from the box).

Lead is variable and probably responds more strongly to spatial position, but epidote is possibly slightly enriched in lead in more Pb-rich granodiorite samples. Epidote in the more felsic samples is generally enriched in strontium but, because of the spatial distribution of lithologies, it is difficult to separate this from any spatial effects. This is illustrated by Zr, which is relatively low in epidote in the more felsic (Zr-rich) host rocks and therefore may reflect a predominant spatial control with proximal epidotes showing depletion in Zr (Fig. 12), similar to its behavior in the Collahuasi district (Baker et al., 2020).

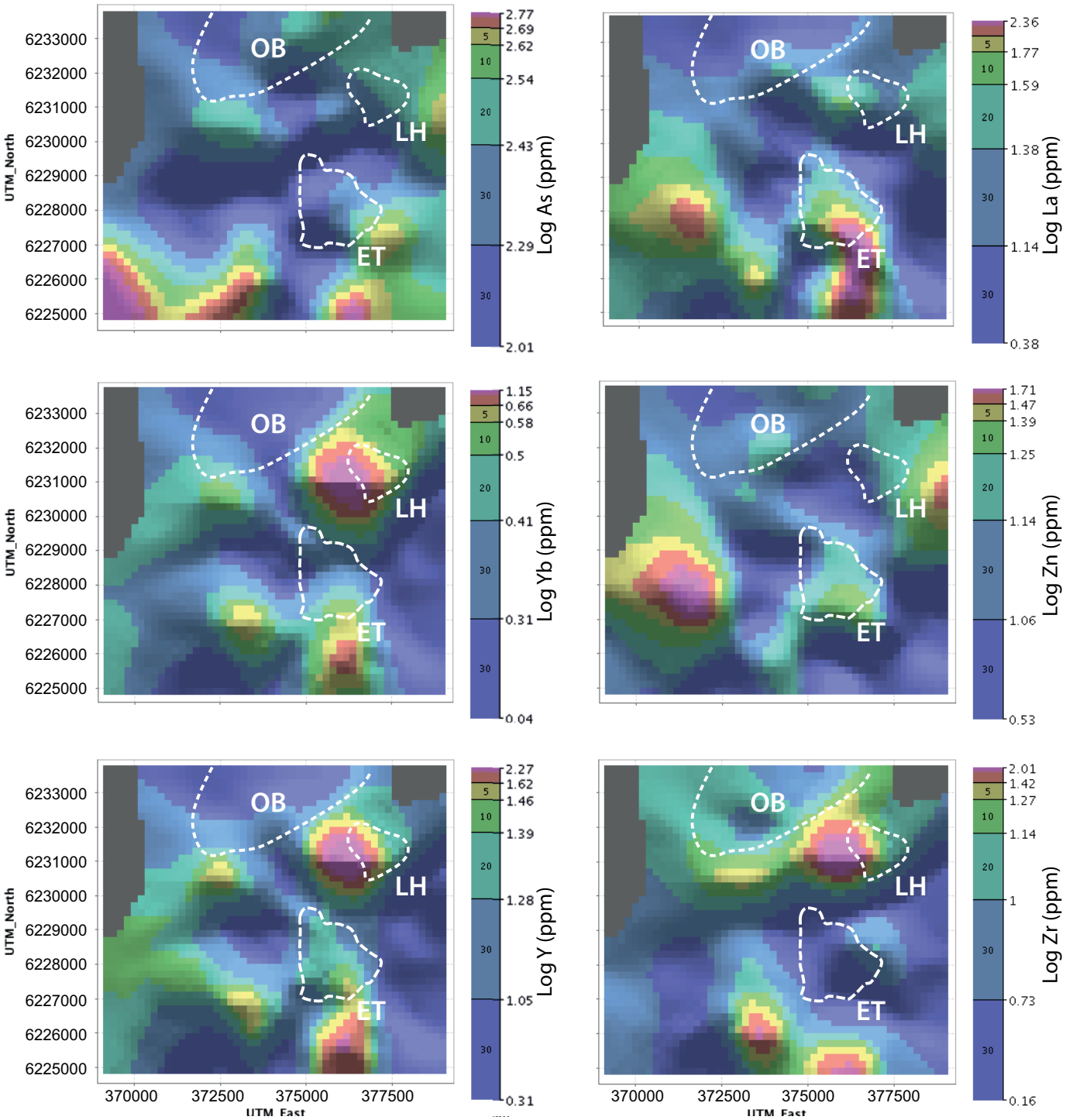

Fig. 12. Gridded epidote compositional data (log of sample average, cell size 200 m, minimum smoothing distance four cells) for trace elements showing proximal lows. Note the apparent slight westward offset between some of the epidote anomalies and the location of the orebody at depth. The El Teniente (ET) dashed line is the 0.5 wt % Cu shell; other dashed lines delineate the appromiate extent of the other alteration systems (LH = La Huifa, OB = Olla Blanca). Color scales show range of values for each element, in percentile bands.

Epidote spatial variations

For the major elements, only Fe shows any systematic spatial pattern, forming a proximal shoulder with a maximum around the edge of the ore shell, somewhat similar to V in chlorite (App. Fig. A4). Systematic patterns are observed for a number of trace elements in epidote, including Cu, As, La, Yb, Zn, Y, and Zr (Figs. 12, 13). A prominent, proximal, positive Cu anomaly overlaps with the ore shell, comparable to the pattern around the Rosario porphyry (Baker et al., 2020), but appears to be offset to the southeast. A second Cu anomaly is located to the west-southwest, related to localized mineralization intercepted in one drill core in the Agua Amarga area that also had elevated trace elements in whole rock (e.g., Fig. 4B-E).

Arsenic displays the most coherent halo (also observed at Ujina; see Baker et al., 2020), with a very broad, butterfly-shaped, proximal low that is offset slightly to the north and west of the orebody and extends for >3 km from the edge of the ore shell. At the limits of sampling there is a suggestion that a distal high is developed. Halo-type anomalies appear to be present for the other elements shown, with peak concentrations reached about 1 to 2 km from the edge of the orebody and with the addition, in the case of Zn and perhaps the REEs, of a small proximal anomaly.

Discussion

A number of mineral chemistry features identified in this study display gradients away from the core of the El Teniente hydrothermal system, as defined by the position of the ore shell. When considering such relationships, it is important to bear in mind the third dimension; on average, the surface samples collected are ~800 m above the level of the center of the deposit as currently mined (Teniente-8, the deepest level is at 1,980 m above sea level) and some are nearly 1,600 m higher, so there is a significant vertical component. Furthermore, the deposit has been tilted, postmineralization, by ~10° to the west (Vry et al., 2010), so that a slight westward offset of the overlying propylitic anomaly might be anticipated. This could be further exaggerated by the topography. Thus, on the west side, the proximal propylitic zone might extend farther, and propylitic grade might be lower on the west side for a given elevation (Fig. 14).

Chlorite vectoring and fertility indicators

Results from chlorite geothermometry confirm that El Teniente sits within a strong thermal anomaly that can be resolved for approximately 2 to 2.5 km beyond the edge of the 0.5 wt % Cu grade contour. This is comparable to that previously observed for Batu Hijau (Wilkinson et al., 2015). As with Batu Hijau, it is noteworthy that the thermal anomaly closely maps the form of the ore deposit itself and is asymmetric in the surrounding propylitic rocks. In the case of El Teniente, there is a steeper gradient to the south. We suggest that this southern boundary is modified by the presence of the Teniente fault zone and the southern boundary of the Sewell diorite, both of which are parallel to the Agua Amarga fault (Fig. 1). Thus, this may reflect a postmineralization offset that has down-dropped the southern block, thereby concealing more proximal propylitic signatures at depth. The data also resolve a second thermal anomaly to the northeast that corresponds to the position of the La Huifa deposit, with lower thermal gradients developed in the area between La Huifa and El Teniente (Fig. 6).

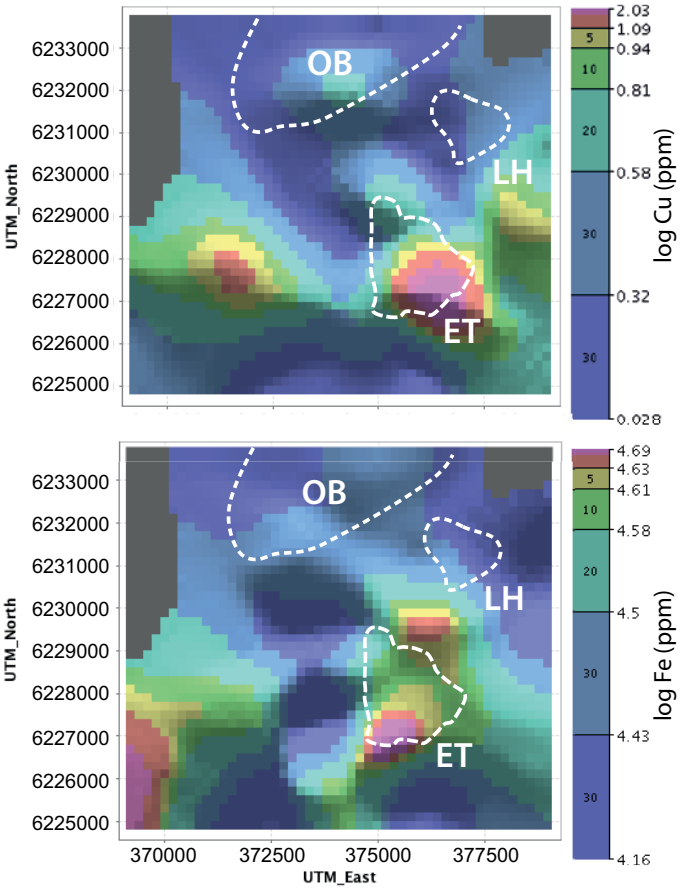

Fig. 13. Gridded epidote compositional data (log of sample average, cell size 200 m, minimum smoothing distance four cells) for trace elements showing proximal highs. The El Teniente (ET) dashed line is the 0.5 wt % Cu shell; other dashed lines delineate the appromiate extent of the other alteration systems (LH = La Huifa, OB = Olla Blanca). Color scales show range of values for each element, in percentile bands.

Chlorite is also enriched in Ti in a bullseye-type anomaly that is coincident with the thermal anomaly (Figs. 6, 8), consistent with the conclusion from Batu Hijau that Ti substitution into chlorite is thermally controlled (Wilkinson et al., 2015). The Ti content of chlorite is a more sensitive vector toward the porphyry center than temperature, because it varies over two orders of magnitude (6–650 ppm). It also defines a gradient that seems to extend out farther laterally, between 1.5 to 2.5 km beyond the upward vertical projection of the ore shell, depending on direction (Fig. 8). There is a distinct westward expansion of the Ti anomaly that could reflect the geometric and geologic factors noted above. Comparable, proximal enrichment of Ti in chlorite is also noted at the Resolution porphyry Cu-Mo deposit (Cooke et al., 2020).

Vanadium in chlorite also shows a proximal anomaly but forms more of a geochemical shoulder that sits on the fringe of the ore shell (Fig. 8)—behavior that is also very similar to Batu Hijau. Outside this shoulder, V gradients extend at least 2.5 km beyond the upward vertical projection of the edge of the ore shell, with the greatest extension again to the west. Although care must be taken not to overinterpret the gridded data, the V map suggests the presence of a west-northwest structural corridor, marked by a pronounced concentration low, be-

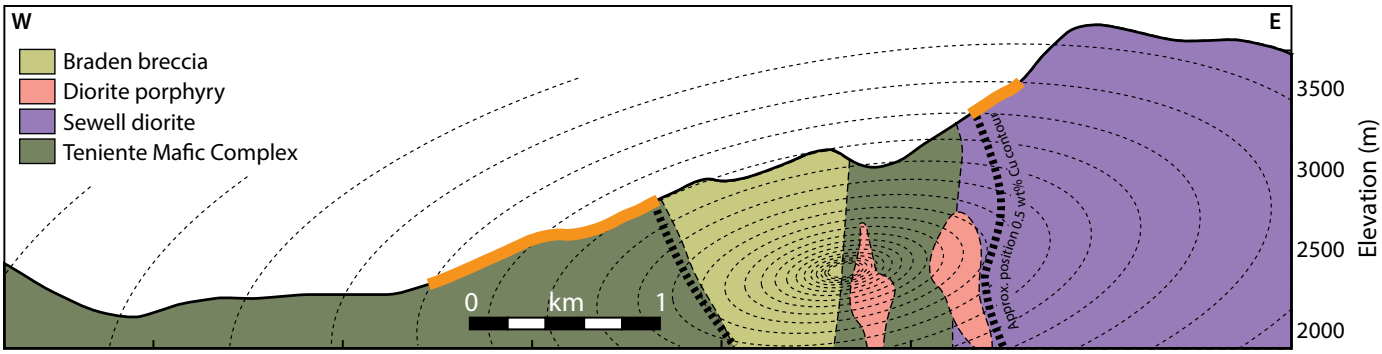

Fig. 14. True scale west-east topographic profile across El Teniente constructed at a northing of approximately 6228000 through the center of the Braden Pipe showing simplified geology. Thick dashed line shows approximate limit of the 0.5 wt % Cu contour. Cartoon representation of propylitic intensity contours to illustrate the potential effects of topography and tilt on mineral chemistry vectors in surface samples. Orange line shows possible greater extent of an inner propylitic zone at surface to the west of the orebody. This asymmetry may be further enhanced by the greater permeability and reactivity of the volcanic rocks of the Teniente Mafic Complex compared to the Sewell diorite.

tween El Teniente and La Huifa (also observed, though less clearly, in the Ti map). This trend is coincident with the Codegua fault, which bounds El Teniente to the northeast (Fig. 1) and is thought to have played an important role in controlling the emplacement of magmas and hydrothermal activity in the deposit, as well as being a long-lived basin-bounding structure that is still active (e.g., O. Rivera and M.F. Falcón, unpub. report, 1998). The Codegua fault is one of many such arc-transverse structures developed along the Andean margin that are thought to reflect reactivation of a pre-Andean basement fabric (O. Rivera and M.F. Falcón, unpub. report, 1998).

A number of elements show proximal lows, with Li being a particularly good example (Fig. 9). This is attributed to mobility of Li (together with Co, Sr, Ca, and REE-Y) in high-temperature potassic and mildly acidic proximal propylitic fluids, as has been constrained by chemical mass transfer analysis in the Northparkes Cu-Au porphyry cluster, New South Wales, Australia (Pacey, 2016). Very similar patterns have also been observed at Batu Hijau (Wilkinson et al., 2015) and at Resolution (Cooke et al., 2020).

As vectoring tools, element ratios in chlorite (proximitor ratios; Wilkinson et al., 2015) are particularly effective because they can enhance significantly the signal gradient around a porphyry center and provide a better discrimination from background. Useful ratios identified at Batu Hijau are shown in Figure 15 for El Teniente, with the addition of V/Li. These ratios vary over three to five orders of magnitude and clearly define the mineralized center of the system. The Ti/Li anomaly is rather remarkable in that it precisely maps the ore shell, including its triangular form, and extends at least 3 km from the edge of the ore shell. This ratio was also very effective in defining the center of the Resolution porphyry system (Cooke et al., 2020). All of the Ti-based ratios, with the exception of Ti/K, clearly coincide with the system center, although Ti/Ni shows a proximal shoulder with the maxima aligning with the 0.5 wt % Cu grade contour. Similar behavior is observed for V/Li. The V/Ni ratio displays an intermediate halo with maxima developed just outside the ore shell to the east but shifted 1 to 2 km away from it in the west and northwest. The distal expression of this pattern arguably extends 5 km from the ore shell in this direction; the same ratio was considered to define one of the broadest halos at Batu Hijau, extending ~5 km from the center of the deposit (Wilkinson et al., 2015).

Significantly, all the Ti-based ratios also show positive anomalies associated with the neighboring alteration-mineralization systems of La Huifa (to the north-northeast) and Olla Blanca (to the north-northwest), with the anomalies appearing to define a connected, lower-intensity corridor. This is similar to the trend noted at Batu Hijau between the deposit and the Sekongkang prospect, interpreted to reflect the geometry of the underlying parental batholith (Wilkinson et al., 2015). For El Teniente, although the propylitic alteration system appears connected between the prospects and deposit, the pattern must be composite, built from overlapping events, given the difference in age of the neighboring systems (Olla Blanca, ~9 Ma; La Huifa, 6.6–6.5 Ma; El Teniente, ~6.3–4.6 Ma).

Plotting the El Teniente data as a function of radial distance from the deposit center shows the same general trends of decreasing proximitor ratios with distance that were observed at Batu Hijau, as exemplified by the Ti/Sr ratio (Fig. 16). A robust regression of the data defines a proximitor equation that predicts distance from the center of El Teniente (X) to an accuracy of ±640 m (1σ):

$$X = \left\{ \frac{\ln(Ti/Sr)}{1607} \right\} / -0.001872 \quad (1)$$

This equation has a slight negative bias, particularly at greater distances, where it tends to slightly underestimate distance to center. Data derived from samples proximal to the La Huifa and Olla Blanca centers plot off this trend, as would be expected if these samples reflect the local anomalies associated with these centers.

The specific characteristics of the chlorite anomalies associated with the two prospects differ in a number of ways from those developed around El Teniente itself (e.g., La Huifa has a proximal V/Ni anomaly, perhaps due to its small dimensions, and both of the prospects are subdued with respect to the Li-based ratios), likely due to different exhumation levels and geologic environments. Olla Blanca is interpreted as an eroded caldera with extensive silification and hot spring activity surrounded by propylitic alteration but with porphyritic intrusions and strong propylitic alteration at depth (Camus, 1977). La Huifa is a

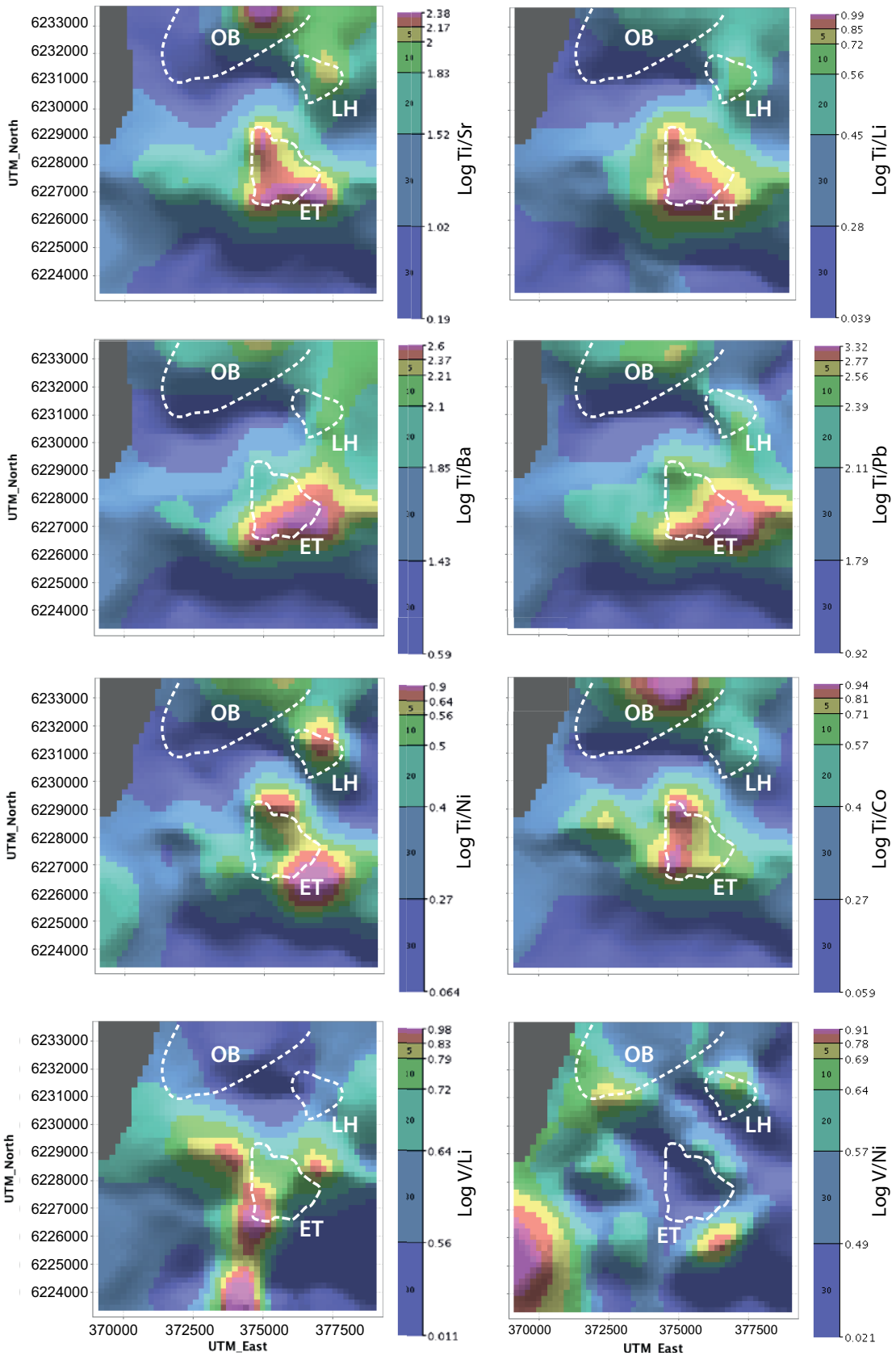

Fig. 15. Gridded chlorite trace element ratios (log of sample average, cell size 200 m, minimum smoothing distance five cells). The El Teniente (ET) dashed line is the 0.5 wt % Cu shell; other dashed lines delineate the appromiate extent of the other alteration systems (LH = La Huifa, OB = Olla Blanca). Color scales show range of values for each ratio, in percentile bands.

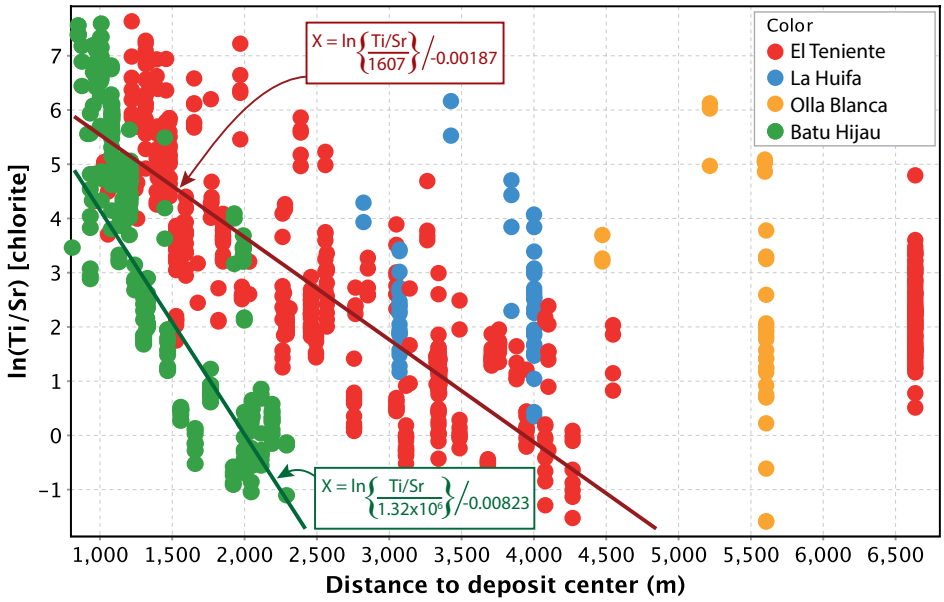

Fig. 16. Plot of the natural log of the Ti/Sr ratio in chlorite as a function of radial distance from the center of El Teniente compared with results from Batu Hijau (Wilkinson et al., 2015). As expected, data from samples proximal to La Huifa and Olla Blanca (shown in yellow and blue) do not follow the trend. Robust linear regression of the El Teniente data (red) produces a reasonable regression fit (R^2 = 0.69) that defines the relationship between Ti/Sr ratio and distance. A new, robust regression of the Batu Hijau data (Wilkinson et al., 2015; data in the range 764–2,300 m, excluding data from the west traverse) gives a good fit (R^2 = 0.84) but with a much steeper slope.

mineralized tourmaline breccia, the Extravío breccia, potentially linked to a porphyry system at depth. From an exploration standpoint, it is significant that the El Teniente anomaly differs significantly from the subeconomic prospects.

The Mg-bearing ratios proposed for Batu Hijau (Mg/Ca and Mg/Sr) do not clearly define the system at El Teniente, probably because of the influence of protolith composition, which can influence the Mg and Fe content of chlorite: very proximal samples at El Teniente are dominated by intermediate to felsic intrusive lithologies as opposed to the basaltic to andesitic composition of the majority of the remainder (App. Table A1).

In terms of fertility assessment, the Mn and Zn contents of chlorite appear to provide a useful guide, being generally rich in porphyry systems. Comparison of the El Teniente data with results from the Baguio district and several background data sets, including some regional metamorphic terranes (Fig. 17), shows that although there is a lot of overlap at low concentration ranges (which tend to be chlorite data from very proximal or very distal locations relative to

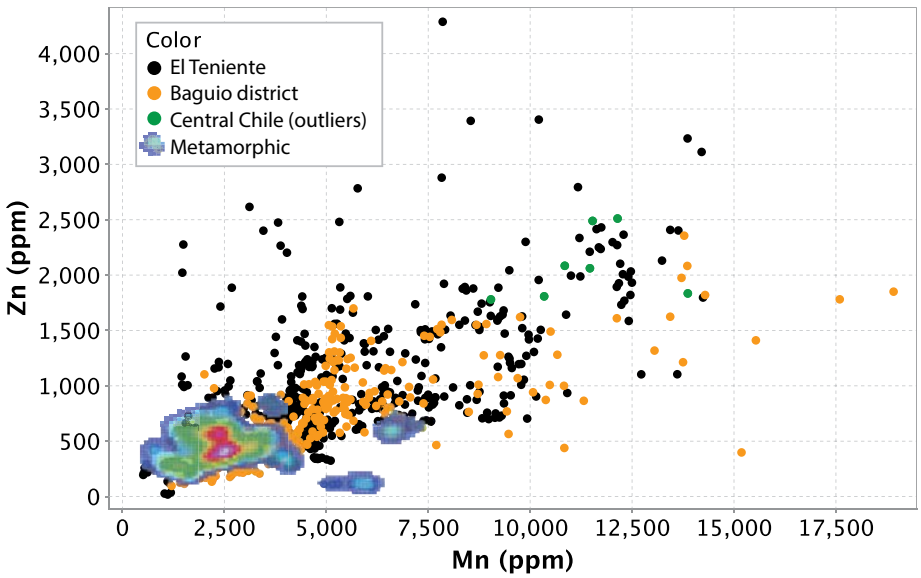

Fig. 17. Zn versus Mn plot for chlorites from the El Teniente area (n = 640) compared with data from the Baguio district (n = 273) and from a variety of metamorphic terranes (n = 457; West Scotland, Georgetown inlier, Harts Range, Central Chile; shown as a point density field), and with a handful of outliers from Central Chile shown as green dots. Data from Wilkinson et al. (2017).

the porphyry centers), it is almost exclusively the porphyry systems that have elevated values, above ~4,000 ppm for Mn and 900 ppm for Zn (also see data from Resolution; Cooke et al., 2020).

Epidote vectoring and fertility indicators

Epidote trace element patterns generally define a broader but less well-defined footprint than chlorite. Arsenic is the best vector element, displaying a broad low in proximity to ore, with a distal enrichment to at least 5 km from the system center, especially to the north and west (Fig. 12). Other elements appear to define a geochemical shoulder, or halo, with maxima at varying distances from the center, but typically at 1 to 2 km from the edge of the ore shell. These patterns are broadly similar to those identified in the Baguio (Cooke et al., 2014b) and Collahusai (Baker et al., 2020) districts. It is noteworthy that the features identified in chlorite that appear to correspond to the La Huifa and Olla Blanca systems are not so evident in the gridded epidote data (Figs. 12, 13).

The most diagnostic features of El Teniente epidote chemistry in relationship to background metamorphic rocks and smaller deposits, such as those of the Baguio district in the Philippines, are the significantly elevated As and Sb concentrations, as well as a general depletion in heavy REEs (Fig. 18). It is noteworthy that the maximum As and Sb concentrations reached in the El Teniente district are broadly similar to, but extend to higher values than, those reported from the Collahuasi district (Baker et al., 2020). Such signatures may therefore be an indicator of super-giant systems, although the possibility of anomalous As and Sb addition in continental arc porphyry systems as opposed to oceanic arcs cannot be excluded, so this relationship may not extend to Cu-Au porphyries developed in island arcs. Nonetheless, it is clear that the significant fluxing of such metals in porphyry-related magmatic-hydrothermal

Fig. 18. Plot of Sb and Yb versus As concentrations in epidote from the El Teniente area in comparison to data from the Baguio porphyry district, Philippines, and several regional metamorphic terranes. Georgetown inlier and Harts Range Proterozoic terrane data from Baker et al. (2017), Baguio data from Cooke et al. (2014b), and West Scotland Paleozoic Moine and Dalradian data from Wilkinson et al. (2017). Note that a large proportion of metamorphic analyses (not shown) were below the limit of detection for As and Sb (typically ~1 ppm for As and 0.1 ppm for Sb).

systems makes the discrimination from regional metamorphic epidote fairly straightforward.

Conclusions

Chlorite and epidote mineral chemistry data from El Teniente support the contention that systematic patterns in propylitic mineral chemistry are developed around porphyry systems that extend up to 5 km beyond the orebody. A range of elements show low concentrations in proximal samples (Li, As, Co, Sr, Ca, and REE-Y in chlorite; As, La, Yb, Zn, Y, and Zr in epidote) that increase toward the fringes of the zone of hydrothermal influence or increase to an intermediate position to form a halo and then decrease to the edge of the porphyry-related propylitic zone. The former are generally effective for discriminating propylitic alteration from regional background signatures, because they are significantly elevated above typical background at the limits of propylitic alteration halos. A number of other elements are high proximal and decrease outward (Ti and V in chlorite; Fe and Cu in epidote). Ratioing proximal high elements to proximal low elements yields values that vary over several orders of magnitude and these define steep gradients toward ore. Not only do mineral chemistry indicators display more robust footprints than conventional whole-rock data (less prone to nugget effects), they also show much better defined and laterally extensive gradients toward ore. These patterns arguably demonstrate a much wider influence of magmatic-hydrothermal fluids in porphyry-related propylitic halos than previously considered, challenging the paradigm that these alteration domains are formed from convecting groundwater. This conclusion is further supported by chemical mass transfer and isotopic data (see Pacey, 2016; Pacey et al., 2020b).

Acknowledgments

We are grateful to CODELCO staff for logistical support of the sampling program and for many insightful discussions. In particular, we thank Alfredo Bertens, Domingo Espiñeira, Ricardo Floody, René Padilla, Alvaro Puig, Fernando Marambio, Jorge Skarmeta, Patricio Zuñiga, and Alberto Galan. We thank Alan Goode and Adele Seymon of AMIRA International and the P765A and P1060 sponsors and research project teams for their contributions to the wider goals of this research initiative. Sarah Gilbert, Leonid Danyushevsky, and Karsten Goemann provided key laboratory support at the University of Tasmania. We are grateful to Dr. Kontonikas-Charos and Dr. Reich for insightful reviews that helped to improve the paper and to Pete Hollings for editorial handling.

REFERENCES

Ahmed, A.D., Fisher, L., Pearce, M., Escolme, A., Cooke, D.R., Howard, D., and Belousov, I., 2020, A microscale analysis of hydrothermal epidote: Implications for the use of laser ablation-inductively coupled plasma-mass spectrometry mineral chemistry in complex alteration environments: Economic Geology, v. 115, p. 793–811.

Astudillo, N., Roperch, P., Townley, B., Arriagada, C., and Chauvin, A., 2010, Magnetic polarity zonation within the El Teniente copper-molybdenum porphyry deposit, central Chile: Mineralium Deposita, v. 45, p. 23–41.

Baker, M.J., Cooke, D.R., Hollings, P.N., and Piquer, J., 2017, Identification of hydrothermal alteration related to mineralisation using epidote mineral chemistry: Society for Geology Applied to Mineral Deposits (SGA) Biennial Meeting, 14th, Quebec City, August 20–23, 2017, Proceedings, p. 1069–1072.

Baker, M.J., Wilkinson, J.J., Wilkinson, C.C., Cooke, D.R., and Ireland, T., 2020, Epidote trace element chemistry as an exploration tool in the Collahuasi district, northern Chile: Economic Geology, v. 115, p. 749–770.

Ballantyne, G.H., 1981, Chemical and mineralogical variations in propylitic zones surrounding porphyry copper deposits: Ph.D. thesis, Salt Lake City, Utah, University of Utah, 208 p.

Bird, D.K., and Spieler, A.R., 2004, Epidote in geothermal systems: Reviews in Mineralogy and Geochemistry, v. 56, p. 235–300.

Camus, F., 1977, Geologia de area emplaziamento de los depositos de cuarzo Olla Blanca, Provincia de Cachapoal: Revista Geologica de Chile, v. 4, p. 43–54.

——2002, The Andean porphyry systems, *in* Porter, T.M., ed., Super porphyry copper and gold deposits: A global perspective, 1st ed.: Adelaide, PGC Publishing, p. 45–63.

Cannell, J., 2004, El Teniente porphyry copper-molybdenum deposit, central Chile: Unpublished Ph.D. thesis, Hobart, Australia, University of Tasmania, 299 p.

Cannell, J., Cooke, D.R., Walshe, J.L., and Stein, H., 2005, Geology, mineralization, alteration, and structural evolution of the El Teniente porphyry Cu-Mo deposit: Economic Geology, v. 100, p. 979–1003.

Cathelineau, M., 1988, Cation site occupancy in chlorites and illites as a function of temperature: Clay Minerals, v. 23, p. 471–485.

Cooke, D.R., Hollings, P., Wilkinson, J.J., and Tosdal, R.M., 2014a, Geochemistry of porphyry deposits, *in* Holland, H.D., and Turekian, K.K., eds., Treatise on geochemistry, 2nd ed., v. 13: Oxford, Elsevier, p. 357–381.

Cooke, D.R., Baker, M., Hollings, P., Sweet, G., Chang, Z., Danyushevsky, L., Gilbert, S., Zhou, T., White, N., Gemmell, J.B., and Inglis, S., 2014b, New advances in detecting the distal geochemical footprints of porphyry systems: Epidote mineral chemistry as a tool for vectoring and fertility assessments: Society of Economic Geologists, Special Publication 18, p. 127–152.

Cooke, D.R., Wilkinson, J.J., Baker, M., Agnew, P., Phillips, J., Chang, Z., Chen, H., Wilkinson, C.C., Inglis, S., Hollings, P., Zhang, L., Gemmell, J.B., White, N.C., Danyushevsky, L., and Martin, H., 2020, Using mineral chemistry to aid exploration: A case study from the Resolution porphyry Cu-Mo deposit, Arizona: Economic Geology, v. 115, p. 813–840.

de Caritat, P., Hutcheon, I., and Walshe, J.L., 1993, Chlorite geothermometry: A review: Clays and Clay Minerals, v. 41, p. 219–239.

Floody, R., and Huete, C., 1998, Potencial Distrito Teniente: Superintendencia de Geología, El Teniente, CODELCO-Chile, 42 p.

Maksaev, V., Munizaga, F., McWilliams, M., Fanning, M., Mathur, R., Ruiz, J., and Zentilli, M., 2004, New chronology for El Teniente, Chilean Andes, from U-Pb, $^{40}Ar/^{39}Ar$, Re-Os, and fission track dating: Implications for the evolution of a supergiant porphyry Cu-Mo deposit: Society of Economic Geologists, Special Publication 11, p. 15–54.

Morel, R.G., 1984, Exploración del Prospecto "Olla Blanca" Temporada Dic. 1983 – Abril 1984: Superintendencia de Geología, El Teniente, CODELCO-Chile, 16 p.

Neal, L.C., Wilkinson, J.J., Mason, P.J., and Chang, Z., 2018, Spectral characteristics of propylitic alteration minerals as a vectoring tool for porphyry copper deposits: Journal of Geochemical Exploration, v. 184, p. 179–198.

Ossandon, G., 1974, Petrografia y alteracion del Porfido Dacitico, Yacimiento El Teniente: Unpublished Honours thesis, Universidad de Chile, 112 p.

Pacey, A., 2016, The characteristics, geochemistry and origin of propylitic alteration in the Northparkes porphyry Cu-Au system: Unpublished Ph.D. thesis, London, Imperial College London, 631 p.

Pacey, A., Wilkinson, J.J., and Cooke, D.R., 2020, Chlorite and epidote mineral chemistry in porphyry ore systems: A case study of the Northparkes district, New South Wales, Australia: Economic Geology, v. 115, p. 701–727.

Pacey, A., Wilkinson, J.J., Boyce, A.J., and Millar, I.L., 2020, Magmatic fluids implicated in the formation of propylitic alteration: Oxygen, hydrogen, and strontium isotope constraints from the Northparkes porphyry Cu-Au district, New South Wales, Australia: Economic Geology, v. 115, p. 729–748.

Pardo, R., 2015, Discovery and geology of La Huifa porphyry Cu-Mo deposit, VI Región, Chile: XIV Congreso Geologico Chileno, La Serena, October 2015, Abstracts, p. 368.

Rudnick, R.L., and Gao, S., 2003, Composition of the continental crust, *in* Holland, H.D., and Turekian, K.K., eds., Treatise on geochemistry, v. 3, The crust: Oxford, Elsevier, p. 1–64.

Sillitoe, R.H., 2010, Porphyry copper systems: Economic Geology, v. 105, p. 3–41.

Skewes, A.M., Arévalo, A.G., Floody, R., Zúñiga, P., and Stern, C.R., 2002, The giant El Teniente breccia deposit: Hypogene copper distribution and emplacement: Society of Economic Geologists, Special Publication 9, p. 299–332.

Spencer, E.T., Wilkinson, J.J., Creaser, R.A., and Seguel, J., 2015, The distribution and timing of molybdenite mineralization at the El Teniente Cu-Mo porphyry deposit, Chile: Economic Geology, v. 110, p. 387–421.
Stern, C.R., Skewes, M.A., and Arevalo, A., 2010, Magmatic evolution of the giant El Teniente Cu-Mo deposit, central Chile: Journal of Petrology, v. 52, p. 1591–1617.
Villalobos, J., 1975, Alteracíon hidrotermal en las andesitas del yacimiento El Teniente, Chile: Unpublished doctorate thesis, Universidad de Chile, 125 p.
Vry, V.H., Wilkinson, J.J., Seguel, J., and Millán, J., 2010, Multistage intrusion, brecciation, and veining at El Teniente, Chile: Evolution of a nested porphyry system: Economic Geology, v. 105, p. 119–153.
Walshe, J.L., 1986, A six-component chlorite solid solution model and the conditions of chlorite formation in hydrothermal and geothermal system: Economic Geology, v. 81, p. 681–703.
Wilkinson, J.J., Chang, Z., Cooke, D.R., Baker, M.J., Wilkinson, C.C., Inglis, S., Chen, H., and Gemmell, J.B., 2015, The chlorite proximitor: A new tool for detecting porphyry ore deposits: Journal of Geochemical Exploration, v. 152, p. 10–26.
Wilkinson, J.J., Cooke, D.R., Baker, M.J., Chang, Z., Wilkinson, C.C., Chen, H., Fox, N., Hollings, P., White, N.C., Gemmell, J.B., Loader, M.A., Pacey, A., Sievwright, R.H., Hart, L.A., and Brugge, E.R., 2017, Porphyry indicator minerals and their mineral chemistry as vectoring and fertility tools: Geological Survey of Canada, Open File 8345, p. 67–77, doi: 10.4095/306305.
Wilkinson, J.J., Pacey, A., Hart-Madigan, L.A., Longridge, J., Cooke, D.R., Baker, M.J., Boyce, A.J., and Wilkinson, C.C., 2019, A new paradigm for the origin of propylitic alteration in porphyry ore systems: Applied Earth Science: Transactions of the Institute of Mining and Metallurgy B, v. 128, no. 2, 1 p.
Zacharias, J., and Wilkinson, J.J., 2007, ExLAM 2000: Excel VBA application for processing of transient signals from laser ablation (LA-ICP-MS) of fluid inclusions and solid phases: Biennial Conference on European Current Research on Fluid Inclusions, 19th, Bern, Switzerland, July, 17–20, 2007, Abstracts, p. 194.

Jamie Wilkinson was born in the United Kingdom and educated at Cambridge (B.A.) and Southampton (Ph.D.) followed by postdoctoral research at Imperial College London. Subsequently, he became a member of faculty at Imperial and became a full professor of geology in 2019, teaching field geology, geochemistry, and economic geology. He has worked on numerous research projects worldwide involving the development of methods for the microanalysis of rocks, minerals, and fluid inclusions and studies of hydrothermal and magmatic ore-forming systems. In 2014, he partly relocated to the Natural History Museum to become a Research Leader in mineral deposits, spearheading the Museum's research initiative in ore deposits research and engaging with the minerals industry via collaborative research projects and consulting. He is cofounder and director of the London Centre for Ore Deposits and Exploration (LODE) and recently held the post of visiting research professor at CODES, University of Tasmania (2008–2010). A focus of current research is the use of mineral chemistry for vectoring and fertility assessment in porphyry-epithermal systems.